Simulation of GPS Radio Occultation Through Sporadic-E Using the Multiple Phase Screen Method

THESIS

Daniel W. Stambovsky, Capt, USAF

AFIT-ENP-MS-20-M-117

DEPARTMENT OF THE AIR FORCE
AIR UNIVERSITY

AIR FORCE INSTITUTE OF TECHNOLOGY

Wright-Patterson Air Force Base, Ohio

AFIT-ENP-MS-20-M-117

SIMULATION OF GPS RADIO OCCULTATION THROUGH SPORADIC-E USING THE MULTIPLE PHASE SCREEN METHOD

THESIS

Presented to the Faculty

Department of Engineering Physics

Graduate School of Engineering and Management

Air Force Institute of Technology

Air University

Air Education and Training Command

in Partial Fulfillment of the Requirements for the

Degree of Master of Science in Applied Physics

Daniel W. Stambovsky, B.S.

Capt, USAF

March 2020

AFIT-ENP-MS-20-M-117

SIMULATION OF GPS RADIO OCCULTATION THROUGH SPORADIC-E USING THE MULTIPLE PHASE SCREEN METHOD

THESIS

Daniel W. Stambovsky, B.S.
Capt, USAF

Committee Membership:

Maj D. Emmons, Ph.D.
Chair

Dr. J. Colman
Member

Lt Col O. Nava, Ph.D.
Member

AFIT-ENP-MS-20-M-117

Abstract

A phase screen simulation experiment is designed and implemented to model radio occultation through sporadic-E ionospheric disturbances between a GPS transmitter operating at the L1 frequency and a second receiving satellite in low earth orbit (LEO). Simulations were made to test the linear relationship between plasma intensity and scintillation S_4 index both posited (Arras and Wickert, 2018) and contended (Gooch et al., 2020) in previous literature. Results brought into question both the linear relationship and the use of S_4 as a whole and an alternate metric was sought. The current work points to two attributes of the low frequency plateau of the spatial Fourier transform of the $|\vec{E}|^2$ intensity as replacements for the the S_4 index. These metrics are shown to have direct relationships to key parameters of the Sporadic-E being simulated, reinforce each other, and have expected behavior under varying plasma conditions. Finally one of the proposed metrics (final peak frequency of the low-frequency plateau) is shown to be highly resistant to noise in the applied signal, and uncovers a promising as a path towards quickly analyzing radio occultation data.

Acknowledgements

It would have been impossible to complete AFIT without the patience, support, and constant encouragement from my wife, an AFIT graduate in Computer Engineering, who could sympathize with all the long hours.

I would also like to thank my thesis advisor, Maj Dan Emmons, for always encouraging me to explore rabbit holes to see what we could pull out of our hats. Your excitement for this research and science in general have made this feel like a true collaboration. I would also like to extend my gratitude to my other committee members, Dr. Jonah Colman and Lt Col Omar Nava for their insights, encouragements, and mission focus. Both of your insights and critical thinking skills has made me a better scientist and me better understand the scientific challenges facing the Air Force.

Finally I must thank my dog Baron who never failed to give encouraging snores while I sat next to him running simulations.

Daniel W. Stambovsky

Table of Contents

List of Figures

List of Tables

I. Introduction

A basic necessity to the accurate transmission of information through a medium is an understanding of how that medium affects the information as it propagates. This is true across all forms of information transfer, be it electrical signals through a cable, photons through fiber-optics, or gravitational waves spreading through the fabric of spacetime. In the realm of radio frequency (RF) intra- or trans-terrestrial wireless communication and sensing that medium is the atmosphere. Within the subset of frequencies in the L-band and below, a key source of signal distortion and propagation path alteration is the concentric bands of stratified atoms and molecules, ionized by the bombardment of high energy solar radiation. As these layers of differentiated chemicals undergo ionization and recombination an altitude dependant plasma density persists producing the stable ionosphere. It has been recognized since the earliest days of radio communication that it is imperative to have at the minimum a broad understanding of the structure and dynamics of this highly variable portion of the atmosphere if the lower frequency bands of the electromagnetic spectrum are to be utilized. The gaseous layer of the earth is, however, notoriously tight-fisted with her secrets, and although considerable progress has been made since signals were first accidentally reflected from the bottom of the E-layer (Joly, 1902), we still lack the observational and theoretical prowess to accurately predict ionospheric conditions with the granularity necessary for exactness in applications such as HF geolocation. These data gaps also prevent the long-term predictive capability to accurately foresee future conditions beyond the fuzziest of estimations.

With the goal of bringing some little clarity to this fog several methods have been devised to measure the state of the ionosphere: sounders (such as the Digisonde) can construct vertical measurements of plasma intensity. While increasingly dense networks of these sensors have been deployed to gain situational awareness, they only

provide localized information on the ionospheric state. Longer range systems in the form of Coherent and Incoherent Scatter Radars (CSR and ISR respectively) exist in a few select locations and have provided essential insight (Hysell, D.L. et al., 2013), but these are few in number and extraordinarily expensive. The first truly global opportunity to study the ionosphere (especially regions of high density, disruptive plasma) came with the launch of satellite constellations. In this arena Global Navigational Satellite Systems (GNSS), especially the US-based GPS system, became an ideal transmitter of opportunity to be used either by the proliferation of ground-based receivers (Maeda and Heki, 2014, 2015; Maeda et al., 2016) or through use of specially designed Constellation Observing Satellite for Meteorology, Ionosphere, and Climate (COSMIC) system and its predecessors. This set of orbital satellites, and its recently launched companion of six additional satellites designated COSMIC II, provide a receive system to pair with GNSS transmitters able to peer through the ionosphere and report on its conditions through a remote sensing technique know as radio occultation (RO). This provides a measurement of signal distortion (scintillation, phase variation, etc.) as it passes through the varying indices of refraction caused by variations in the electron content of the ionosphere. RO can also be used for analysis of neutral atmospheric conditions that affect RF propagation (see https://www.nesdis.noaa.gov/COSMIC-2 (2020)).

Data collection is, however, only half the battle. Analysis of the collected information, and converting that information into a picture of the ionospheric state is often far from trivial. When it comes to RO measurements of ionospheric disturbances an effective analysis will provide a metric that correlates signal disruption to specific properties of the plasma through which it traveled. The scintillation index, S_4, is a frequently used method to do exactly that, and Arras and Wickert (2018) shows a linear relationship between plasma strength of sporadic-E type disturbances and S_4.

Attempts to reproduce this relationship with larger data sets by Gooch et al. (2020), however, have struggled and hint at a far more complex interaction at work. Thus the scintillation index may have some severe limitations, a breach in analytic capability that needs to be filled by some other metric. This document attempts to fill this void, and thus address a small piece of the large and dauntingly complex effort to build an overall picture of ionospheric processes.

To see how the current work fits into the overarching puzzle, some background is required to situate the research. Although typically less intense than the strong F2 peak of ionospheric intensity, the E-layer plays a key role in ionospheric impacts on RF transmissions for two important reasons: first, it is physically lower in altitude (100-150 km while the F-layer is 150 km and up) so is the first to interact with ground based transmissions. For RF frequencies below the blanketing frequency (fbEs) will be entirely reflected by this layer. Secondly, the E-layer is often highly unpredictable with clouds of high fbEs (a measure of plasma intensity directly related to the electron density) values caused by long lived metallic ions whose drifting movement is just beginning to be explored (Maeda and Heki, 2015). The difficulties in measurement suggest simulation may be a useful stand-in in the search for a series if parameters that can be matched to data from RO measurements. There is an extended body of work stretching back to the mid 20th century attempting to do exactly this, and the current work adds to that body. It does so by reproducing the multiple phase screen (MPS) approach of simulating geographically extended RF-plasma interactions as seen in Knepp's multitudinous publications (Knepp, 1982, 1983, 2016) and used to good effect by Zeng and Sokolovskiy (2010). Standing on their shoulders the current work proposes two new metrics and explores how (in simulation) they reflect key parameters in sporadic-E atmospheric plasmas.

II. Background

As with all atmospheric phenomena, the features and behaviors of ionospheric structures are the result of a web of interconnected and interdependent causes and effects. While this woven structure of relations tempts the desire to spurn any but a holistic, emergent description, the sheer size and complexity of the ionosphere make the results of such attempts at best approximate. As a result we are forced to turn to a bottom-up approach, gleaning what information we can about various features while keeping careful note of the assumptions made along the way. The purpose of this chapter is to frame the document as a whole, building a baseline understanding of the physical structure of the ionospheric disturbances known as Sporadic-E and the most common methodology for simulating their interactions with Radio Frequency (RF) signals. First, this chapter provides background on Sporadic-E and its place in the ionospheric environment. Secondly, it provides an overview of the phase screen method of simulating RF-plasma interactions, it's use in exploration of Sporadic-E properties is justified, and the mathematical methodology and assumptions are derived.

2.1 Ionospheric Structure

The gross structure of the ionosphere has been known for decades and is well described in literature (Schunk and Nagy, 2009). Starting at approximately 100 km, the distribution of standard constituents in the atmosphere begin to stratify by mass. Heavier atoms and molecules decrease in concentration geometrically with increasing altitude building layers each with a dominating concentration of a particular element or molecule. This structure, in turn, produces various photoionization and recombination rates from solar ultraviolet (UV) and X-ray emissions. The altitude

dependant rate of electron-ion pair generation from and recombination back to neutral constituents in the upper atmosphere produces the characteristic electron density curve seen in Figure 1.

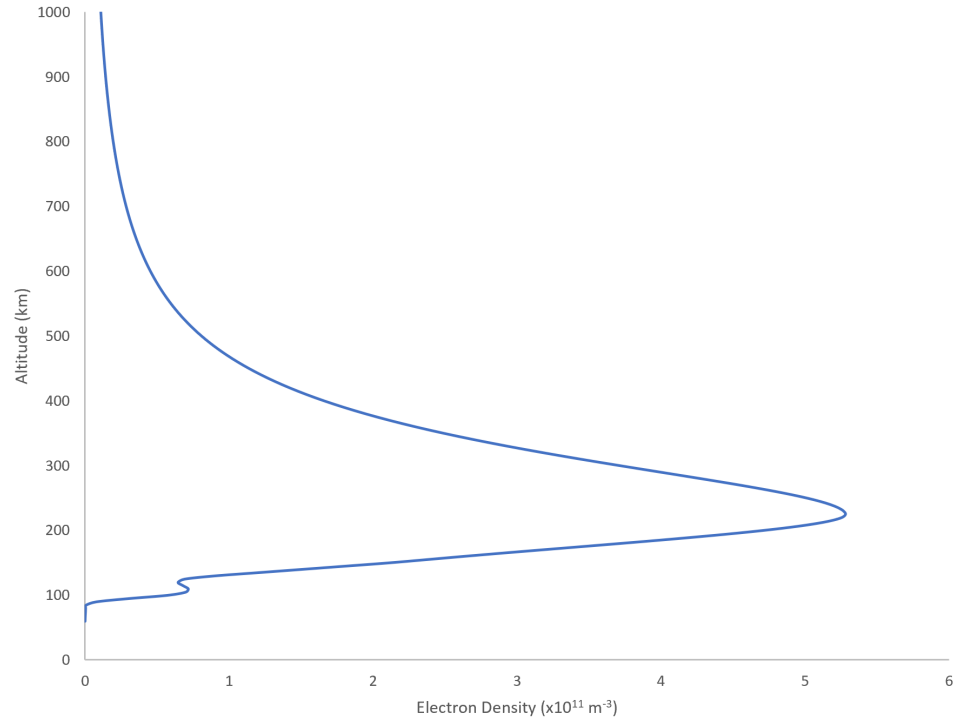

Figure 1. Representational structure of the ionosphere in a idealized state in the northern hemisphere mid-latitude summer at local noon as represented by electron density. Note the peak in the E-layer at just about 100 km. Data was generated using the International Reference ionosphere model.

The ionosphere is typically split into three main layers which are in order of increasing altitude: the D-layer from 60-100 km, the E-layer ranging from 100-150 km and the F-layer from 150 km to the top of the ionosphere. All of these layers can shift in altitude and intensity based on both cyclic influences (i.e. time of day, time of year, sunspot cycles) as well as random events such as traveling ionospheric disturbances (TIDs) and solar storms (Schunk and Nagy, 2009). Of primary interest to this work is the E-layer which is seen in Figure 1 as the small bump in electron density at approximately 100 km, which is situated above the complex chemistry of

the D-layer and below the F-layer's large F2 peak (seen in this Figure 1 at about 240 km). The E-layer is unique in that it is subject to long-lasting, highly unpredictable disturbances known as sporadic-E. These clouds of high-density plasma can cause the E-layer to locally dominate ionospheric radio impacts (Maeda and Heki, 2014). As with other ionospheric disturbances, sporadic-E can cause unexpectedly low altitude High-Frequency (HF) radio reflections, Over the Horizon Radar (OTHR) inaccuracies (Thayaparan et al., 2019), and phase delays or timing errors in Global Navigation Satellite Systems (GNSS) systems (Maeda et al., 2016). These make research into sporadic-E of high interest to a variety of academic and engineering disciplines, and motivates the current work.

2.2 Sporadic-E Properties and Measurement

Given the potential impact of ionospheric disturbances on communication, sensing, and navigation there is interest in understanding the state and processes of change within the ionosphere. Unfortunately, as with the neutral atmosphere, the ionosphere is a complex, chaotic system that is not easily measured or modeled. Even focusing in on a single class of disturbance, the sporadic-E, there are a slew of competing theories of generation mechanisms, and knowledge of their shape and prevalence is far from complete (Maeda and Heki, 2015; Whitehead, 1989).

2.2.1 Sporadic-E Origin and Form

For mid-latitude sporadic-E, where much experimental work has taken place, the prevalent theory of sporadic-E generation is neutral vertical wind sheer crossed with the prevalent geomagnetic field creates a $\vec{u}_n \times \vec{B}$ force (using terminology from Schunk and Nagy (2009) with $\vec{u}_n$ being zonal winds) which concentrates long-lived metallic ions (especially Fe^+, Mg^+, Ca^+, and Na^+). The ions are ablated in neutral form

from meteors traveling through the atmosphere and then photoionized before being compressed into thin sheets at an altitude of approximately 100 km by the aforementioned mechanism. Since the dissociative recombination rates of these ions are orders of magnitude less than atmospheric neutrals (see McNeil et al. (2001) for comparative reaction rates) the prevalence of these ions can overshadow the effect of solar UV and soft X-Ray ionized O_2 and N_2 by an order of magnitude. This results in extremely high electron densities in localized thin sheets (Denardini, C.M. et al. (2016), Whitehead (1989), Maeda and Heki (2015), Mathews (1998), for alternate day and night sporadic-E formation methods see Maeda et al. (2016)). The coarse structure of sporadic-E (scales of tens of km and larger) has been experimentally explored for decades using radar, sounders, TEC detectors, and (of most importance here) various forms of satellite radio interference (Hysell, D.L. et al., 2013). These efforts have yielded a fair understanding of gross morphology and dynamics, as explored in the expansive study of mid-latitude sporadic-E morphology by the Japanese researchers led by Jun Maeda (Maeda and Heki, 2014, 2015; Maeda et al., 2016) using GPS receivers and satellite-based L-band synthetic aperture radar (SAR). The fine structure, however is just beginning to be uncovered through Incoherent Scatter Radar

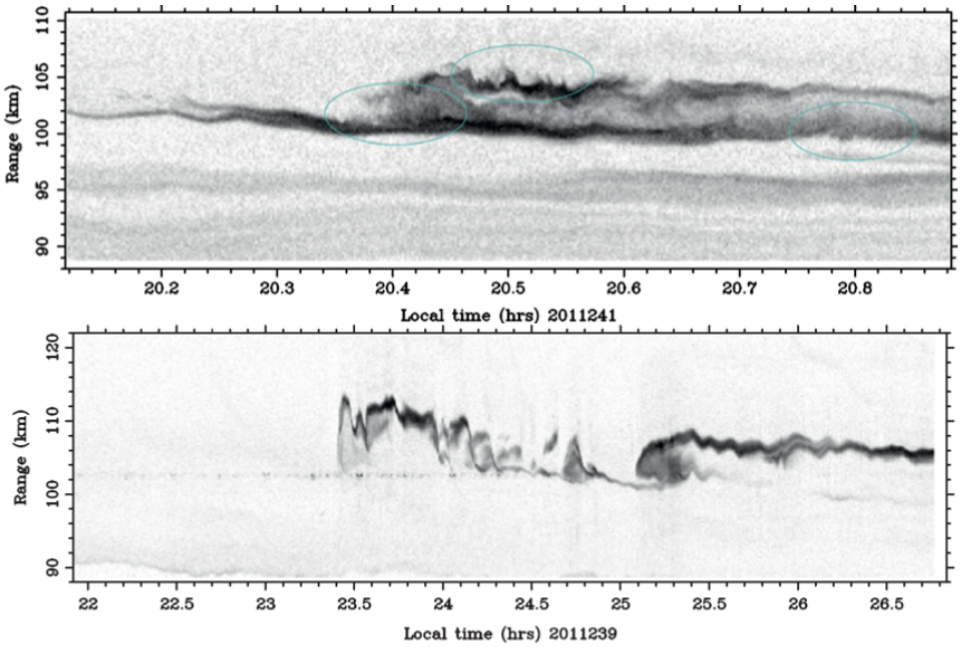

Figure 2. Incoherent Scatter Radar (ISR) images of two separate sporadic-E events made by Arecibo Observatory August 27 (bottom) and 29 (top) 2011. Note the duel layer structure on the top image suggesting a second sporadic-E formed on top of a previous making a channel of low ion density between the two. Additionally Helmholtz instabilities on the top cloud have been circled (annotations original) displaying the complex small-scale structure. Additionally both images display a single thin line of high intensity in close proximity to more diffuse regions above or below. From Hysell, D.L. et al. (2013), used with permission.

The complexity of this structure is extensively discussed in its source paper (Hysell, D.L. et al., 2013), with many of the small Helmholtz instabilities having their origin in the wind sheer that helps construct the sporadic-E. The degree to which these small-scale structures impact passing RF signals is far from settled, but would depend strongly on the ratio of the signal wavelength to structure size, direction of propagation, and probably a host of other considerations. Simulation of these effects (perhaps with full-wave electromagnetic simulation techniques) would be important to understanding these interactions, but is beyond the scope of this document.

2.2.2 Electron Density and Blanketing Frequency

Plasma intensity is typically measured in terms of electron density, but this is, in most cases, not directly measured in the atmosphere. Instead it is the manner in which the plasma effects the propagation speed of electromagnetic waves at particular frequencies, that is the index of refraction, whose effects are measured. On the micro scale a free electron can be displaced by the electric field into a non-equilibrium state, as that field varies over time the electron's inertia and interaction with surrounding charges (and external magnetic fields) produce an harmonic motion known as the plasma frequency. The electron density has a direct effect on two key parameters needed to describe the plasma-RF interaction: firstly the electron-neutral collision frequency

$$\nu = \frac{54.5}{\sqrt{2}} \left(\frac{n_e}{10^6 T^{\frac{3}{2}}} \right), \tag{1}$$

where n_e is the electron density and T is the temperature. Secondly the electron density helps determine the the plasma frequency

$$\omega_p = \sqrt{\frac{e^2 n_e}{\epsilon_0 m_e}}, \tag{2}$$

with e being electron charge, m_e its mass, and ϵ_0 the permittivity of free space. These play into the Appleton-Hartree formula (named for some of the early investigators of ionospheric phenomena) to give the index of refraction of a plasma in its interaction with a signal of frequency ω

$$n^2 = 1 - \frac{X}{1 - iZ - \frac{Y_T^2}{2(1-X-iZ)} \pm \sqrt{\frac{Y_T^4}{4(1-X-iZ)^2} + Y_L^2}}, \tag{3}$$

where:

$$X = \frac{e^2 n_e}{\epsilon_0 m_e \omega^2} = \frac{\omega_p^2}{\omega^2}, \tag{4}$$

$$Z = \frac{\nu}{\omega}, \tag{5}$$

$$Y_L = \frac{\omega_L}{\omega}, \tag{6}$$

$$Y_T = \frac{\omega_T}{\omega}, \tag{7}$$

(Davies, 1990). Here Y_T and Y_L are as a result of the transverse and longitudinal magnetic field with a corresponding gyro-frequency ω_T and ω_L (these magnetic effects are not directly calculated for these simulations and are merely subsumed into the simulated index of refraction). The index is thus dependant on both the signal frequency and the ratio of the plasma frequency (thus electron density) to signal frequency. Given all of these interrelations it would be ideal to know the electron density at each point in space to understand how the ionospheric plasma will interact with the RF signal. It is, however, practically difficult to determine density at each point in the atmosphere. While radar measurement methodologies such as ISR or ionosonde are able to observe localized electron content there are limitations to even these systems. It is from the ionosonde readings that a measure of sporadic-E intensity, the blanketing frequency (fbEs) emerges.

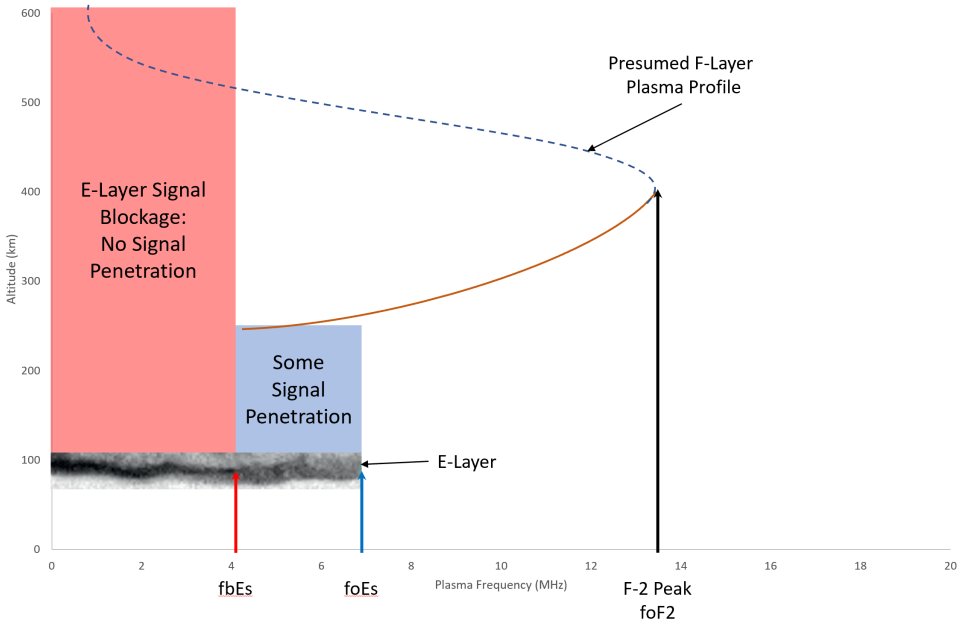

Figure 3. Blanketing frequency for the E-Layer (fbEs) is the frequency below which it blocks all signals. Between fbEs, below foEs, is a region which, although it may have spotty areas which block signal propagation, on the whole it is unable to completely block RF passage and some signals may get through. It is worth noting that in areas of signal blockage (either from the E-Layer or F-Layer) no data may be collected from the ground using RF of these frequencies.

For the simulations in the present document the intensity of the E-Layer (and simulated sporadic-E) will be fbEs measured in MHz. For any transatmospheric measurements (such as RO methodologies) the only information encoded into the signal by its passage through any number of disturbances is the sum total of all path interactions. This is why total electron content (TEC), that is the integrated electron density along a path length, is a common metric used in measurements of ionospheric disturbances (See Hocke et al. (2001) among others). For simulations of the type used here, however, it is the localized index of refraction about a specific phase screen that is the necessary metric, fbEs is utilized as an electron density stand-in.

III. Methodology and Results

We have been left with a problem, localized radar measurements have shown the complex structure of Sporadic-E, but RO measurements with a more global reach lack necessary resolution. What's more, despite the prevalence of GNSS and COSMIC satellites a common metric of RO measurements (S_4) seems to be insufficient to classify Sporadic-E. The purpose of this chapter is to put forward a possible step toward a solution. It explicates the derivation of the parabolic approximation of the wave equation, and the implementation of its numeric solution through the multiple phase screen method. This long-standing approach of simulating RO of a simplified Sporadic-E is used to suggest an alternate metric which may bypass the issues with the standard use of S_4 calculation for classifying fbEs and other properties of the plasma cloud. The results of a series of simulations will highlight the potential of this method and suggest a path towards its application to measured RO events.

3.1 Parabolic Wave Equation

The mathematical mechanism of phase screen simulation is a numeric iterative approach to solving a simplified variant of the Helmholtz scalar wave equation. Originally described in 1946 (Leontovich and Fock, 1946), the simplifications applied to wave propagation allow solutions to be numerically simulated with a great reduction in processing power compared to full-wave processes e.g. Finite Difference Time Domain (FDTD) or Method of Moments (MoM). The phase screen parabolic approach can thus be applied to problem sets that would be prohibitively large for FDTD or MoM methods, making it ideal for ionospheric modeling where the modeling region is measured in hundreds or thousands of kilometers. It behoves us then to derive the parabolic equation so as to explicitly highlight both the strengths and weaknesses of

this approach. Following the process seen in Knepp (1982, 1983, 2016); Levy (2000), we can start with a few explicit assumptions: 1) since the phase screen will be simulated in a two dimensional plane we can pick either the $\vec{E}$ or $\vec{B}$ field rather than the interaction between the two vector fields as in the FDTD Yee cell and we can thus define a generic field term $\Psi(x,z) = e^{ikx}\psi(x,z)$, usually taken as the electric field. 2) Homogeneity of the propagation medium in the direction of travel is assumed, although explicitly known not to be the case as this is precisely what causes perturbations in the RF signals. It is assumed, then, that the rate of change of index of refraction of the medium is small to enable use of the Helmholtz scalar wave equation. With these assumptions in hand we begin with the Helmholtz equation

$$\left(\nabla^2 + k_0^2\epsilon_r(\vec{r})\right)\Psi = 0 \tag{8}$$

where k_0 is the wavenumber and $\epsilon_r(\vec{r})$ is the permitivity of the medium at some position $(\vec{r})$. As it stands, however, we require knowledge of two sets of boundary conditions in advance to solve this equation: vertical ($\pm z_{max}$ and in the direction of propagation ($\pm x_{max}$). A paraxial wave equation is used to reduce the complexity of the Helmholtz solution, allowing the simulation to run with only an initial condition (the injected planewave) at $x = 0$.

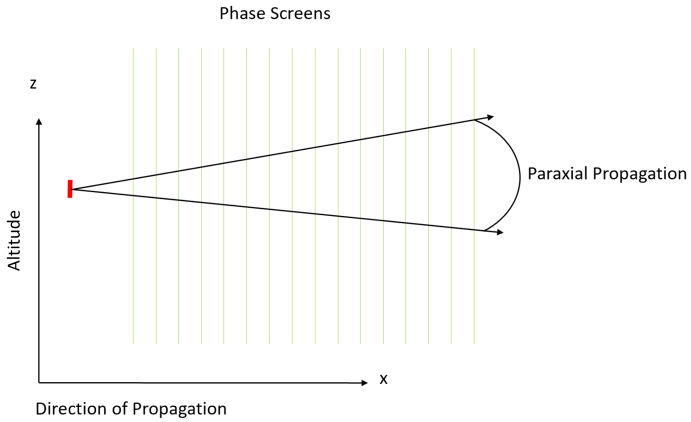

Figure 4. Visualization of paraxial propagation of a source through the simulation area, note the preferential directionality in x avoiding the altitude boundaries in z. This provides an added bonus of eliminating the need for building absorbing boundary conditions into the simulation at $\pm z_{max}$.

The preferential propagation seen in Figure 4 requires the removal of the rapid phase oscillations to eliminate swift, cyclic variations in the direction of propagation. To do so a reduced wave construct is built

$$u(x,z) = \Psi(x,z) * e^{-ikx}. \tag{9}$$

This eliminates the need of tracking 2π worth of phase change every 20 or so centimeters across 2000 or more kilometers; the net phase change between screens will be calculated later. When inserted into the two dimensional version of the Helmholtz equation the reduced wave construct yields

$$\partial_x^2(u) + 2ik\partial_x(u) + \partial_z^2(u) + k^2\epsilon_r(\vec{r})u = 0. \tag{10}$$

Using Assumption 2 the permittivity is taken to be constant in x for each point in z between any two screens, so vectorial aspect of this term is dropped. Instead it is replaced with index of refraction ($n = \sqrt{\frac{\epsilon_r}{\epsilon_0}}$) at each point in z on the screen which is

assumed as a constant integrated value between screens. Alternately a plasma specific property such as plasma frequency or electron density may be used as a stand in to permittivity as it is intimately connected to these properties.

To analyze the details of the paraxial approximation, radiation from an ideal dipole is analyzed with field strength:

$$|\vec{E}| \propto \frac{e^{ik|\vec{r}|}}{|\vec{r}|}. \tag{11}$$

For large distances away from the dipole oscillator, the praxial approximation can be explicitly applied using a small angle approximation to the position vector $\vec{r}$ in Figure 5.

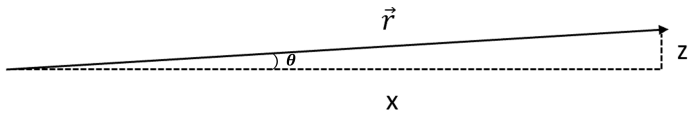

Figure 5. Small angle (θ) in the x-z coordinates required to allow the paraxial approximation. Within the phase screen simulation this correlates to small divergence in the z (altitude) direction.

Explicitly

$$|\vec{r}| = \sqrt{x^2 + z^2} = x\sqrt{1 + \frac{z^2}{x^2}} \approx x + \frac{z^2}{2x} \tag{12}$$

Replacing $|\vec{r}|$ in the dipole as equation and returning to the reduced wave construct function u yields

$$u(x,z) \propto \frac{e^{ik\left(x+\frac{z^2}{2x}\right)}}{x + \frac{z^2}{2x}} e^{-ikx} = \frac{e^{ik\left(\frac{z^2}{2x}\right)}}{x + \frac{z^2}{2x}} \tag{13}$$

When this field is placed into the two dimensional Helmholtz equation above it can be shown that

$$\partial_x^2(u) << \partial_z^2(u) \quad \text{and} \quad \partial_x^2(u) << \partial_x(u). \tag{14}$$

This allows $\partial_x^2(u)$ to be dropped from the Helmholtz equation finally giving the

parabolic wave equation that is to be solved through the phase screen process

$$\partial_z^2(u) + 2ik_0\partial_x(u) + k^2\epsilon_r(\vec{r})u = 0. \tag{15}$$

There is one more approximation inherent in this formulation, following Levy (2000) (who utilizes the index of refraction n instead of permitivity ϵ_r) Equation 10 can, with the caveat of Assumption 2, be conditionally factored as

$$\left[(\partial_x + ik(1-Q))\left(\partial_x + ik(1-Q)\right)\right](u) = 0. \tag{16}$$

Which is in turn broken into a coupled system of two different differential equations with coupled solutions $u_+(x,z)$ and $u_-(x,z)$

$$\partial_x(u) = -ik(1-Q)(u) \quad \text{and} \quad \partial_x(u) = -ik(1+Q)(u), \tag{17}$$

where Q is the psudo-differential operator defined as

$$Q(Q(u)) = \left(\frac{1}{k^2}\partial_z^2 + n^2\right)(u). \tag{18}$$

The solution to this differential equation is a set of functions $u(x,z)$. These are separated into two groups corresponding to the forward and rearward (that is $+x$ and $-x$) propagation terms, i.e. forward propagation and reflection. The paraxial approximation outlined above serves to solve the forward propagation independently meaning that the phase screen technique used here does not solve for reflected energy of the planewave that strikes the plasma. The importance of this simplification is explained in depth in Levy (2000), essentially it has reduced the order of the elliptical Helmholtz equation, reducing not only the boundary conditions, but the dimensionality of the mesh necessary to generate a solution and greatly easing the computational

complexity.

3.2 Phase Screen Derivation

The multiple phase screen method of simulating electromagnetic (EM) signal propagation functions by numerically solving the parabolic equation outlined above. This method is well described in past work (Knepp, 1983; Levy, 2000; Rino, 2011) and determines the solution to the parabolic field equation at some step x_2 in terms of the field at the previous step x_1 which is behind x_2 by a length Δx. Explicitly this relationship is

$$u(x_2, z) = e^{ik\Delta x(Q-1)} u(x_1, z). \tag{19}$$

Functionally this solution can be broken into two parts, each represented by a different phase advance: the first due to traveling through a medium with a varying index of refraction over a distance Δx (which is compressed to a phase addition at the each screen), and the second phase progression from advancing from screen to screen. To collapse the effect of the phase change from the varying index of refraction term (built into the Q above) it is integrated over the distance dx between two screens in the manner of geometric optics

$$e^{-ik\phi} \quad \text{where} \quad \phi = \int_{\frac{-dx}{2}}^{\frac{dx}{2}} n(x', z) dx'. \tag{20}$$

This develops the phase accumulated between two screens at any point in altitude z based on the material between the screens while maintaining the requirements of Assumption 2. It should be remembered that in plasma applications, such as ionospheric RO, the index of refraction is directly related to the electron density.

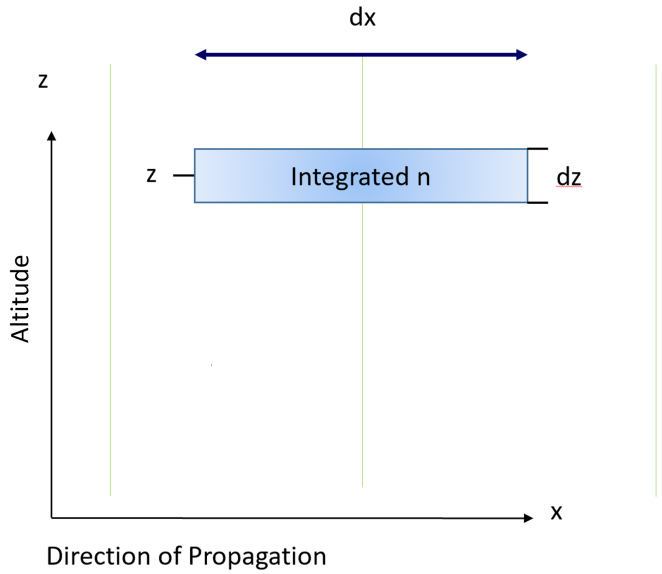

Figure 6. Index of refraction integrated to build the phase offset ϕ on the central screen. While this theoretically can be continuous in z, in implementation the altitude is meshed into units of width dz. It is clear from this process that the smallest resolvable structure of the plasma that is being simulated with the phase screen method is on the order of dx by dz.

With a phase addition from the varying index of refraction in hand we turn to the physical travel distance between phase screens. In Figure 6, for example, this distance is between the leftmost screen and the central screen and is also a distance of dx. The most common way of performing this (see Levy (2000), Knepp (1983), and Rino (2011) among others) is to take the spatial transform in the direction perpendicular to travel, here z, convolve the phase of travel along dx and reverse transform at the next screen. Taking the left screen in Figure 6 as having position x_1 and the center screen having position x_2 the phase change from x_1 to x_2 is calculated first by transforming the field at x_1

$$\tilde{u}(x_1, \kappa) = \frac{1}{2\pi} \int_{-\infty}^{\infty} u(x_1, z) e^{i\kappa z} dz, \tag{21}$$

where κ is the transform variable pair to z, and $\tilde{u}$ is the transformed pair to u.

Advancing the phase over dx is achieved by

$$\tilde{u}(x_2, \kappa) = \tilde{u}(x_1, \kappa) e^{-i\kappa^2 \frac{x_2 - x_1}{2k}}. \tag{22}$$

Now the reverse transform of $\tilde{u}(x_2, \kappa)$ is taken to return the field at the center screen located at x_2

$$u(x_2, z) = \int_{-\infty}^{\infty} \tilde{u}(x_2, \kappa) e^{-i\kappa^2 \frac{x_2 - x_1}{2k}} e^{-i\kappa z} d\kappa. \tag{23}$$

This whole two-part process works functionally as follows: the wavefront starts at x_1, it is propagated to point x_2, the compressed phase alterations from the integrated index of refraction is added at x_2, and then wavefront is then propagated again to the next screen x_3. This process may be continued as necessary until the entire simulation area has been covered. Note that the distance represented by dx need not be constant through the simulation region so, for example, a large area that has no variation in index of refraction may be simulated via a single large screen separation. The method employed does not explicitly set boundary conditions at $+/-z_{max}$ (e.g. Perfectly Matched Layers), instead it relies on the small angle approximation an undisturbed plane wave will propagate only in the $+x$ direction. Implicitly, however, the continuity boundary requirements built into the wave equation can come into play if the field at the points directly adjacent to the boundaries propagates into them. For most sporadic-E intensities the size of the simulation area in the z direction is large enough that any relatively small divergence from this typical mode of propagation has a small enough angle that the final screen is well before energy diffracted in the z direction would reach the boundaries. If the simulation area is narrowed, however, or extremely high plasma intensities are used the simulated field can reflect off the boundaries in a non-physical manner causing simulation error (Figure 7).

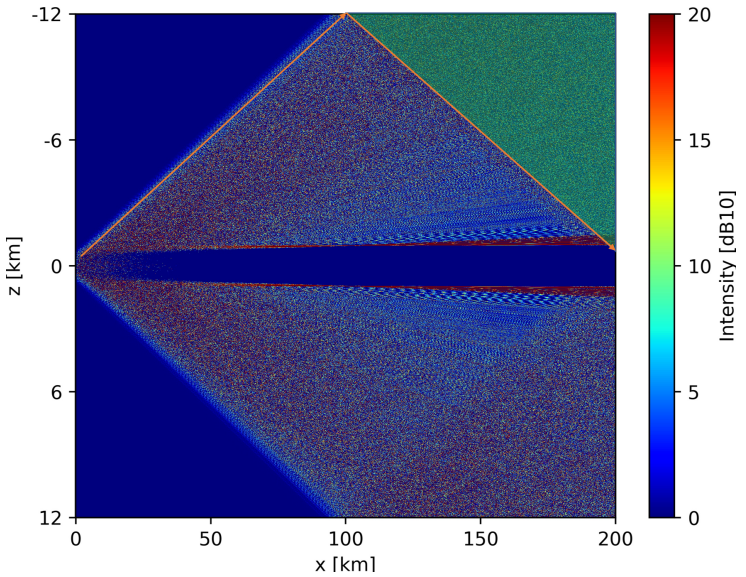

Figure 7. Field intensity plot showing reflection off top and bottom z boundaries as a result of high-frequency (high electron density) plasma. The area containing reflections from the upper boundary is highlighted by a green triangle, and a sample ray has been traced with orange arrow.

3.3 Simulations

3.3.1 Phase Screen Validation

In order to test the developed code and ensure it was providing realistic results, it was first evaluated using a deterministic Gaussian phase-lens on the first screen. This is a method seen previously in Knepp (1983) as a method to compare the results of the code to a known analytic result. The lens is of the typical form

$$\phi(z) = \phi_0 e^{\frac{-z^2}{r_0^2}} \tag{24}$$

which can be manually propagated a distance equivalent to the simulation area using the Fourier method described in Section 3.2 above. The result of this analytic solution was compared to the fully simulated plane wave distorted by the same lens and

propagated via the multiple phase screen method.

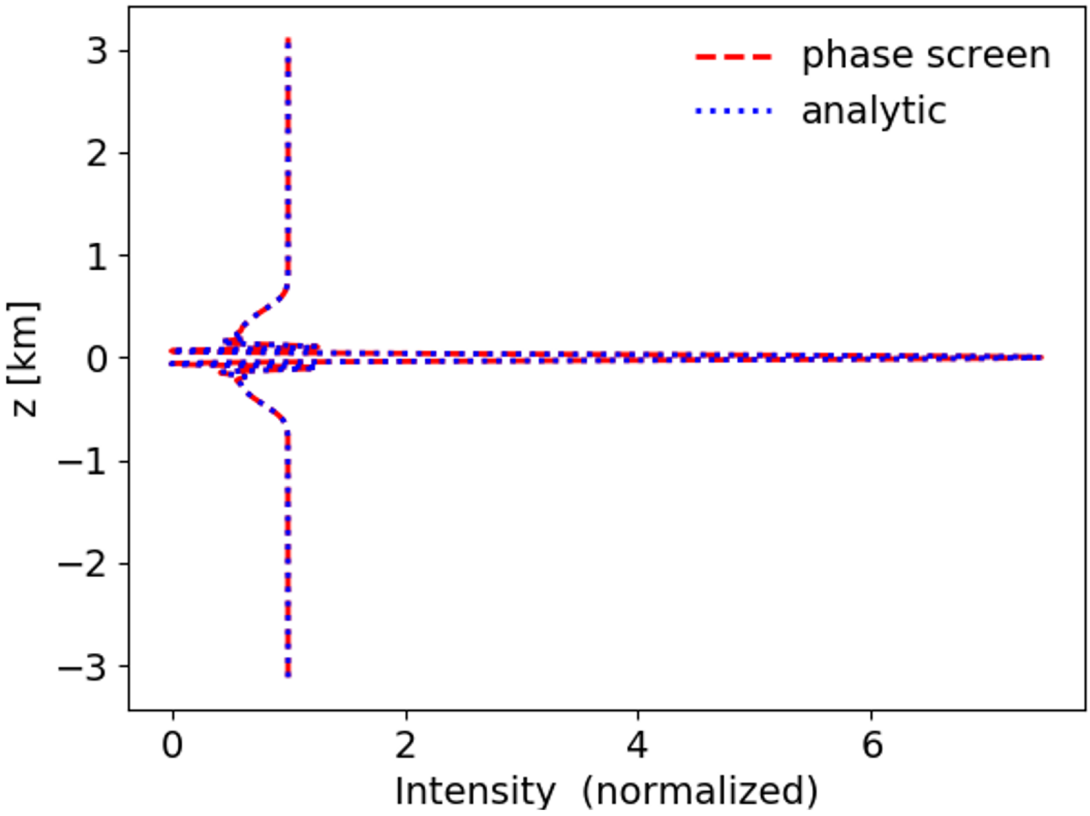

Figure 8. Gaussian lens test of the multiple phase screen code used for the current work. The analytic solution and fully simulated solution can be seen to overlap giving high confidence in the code's ability to perform within the known parameters of multiple phase screen restrictions.

With the first test of the code successfully completed we moved on to comparing the current code to previously published results using a similar methodology. Zeng and Sokolovskiy (2010) implement a series of simulations through sporadic-E representative atmospheric plasma using a phase screen and provides all of the parameters necessary to emulate their results.

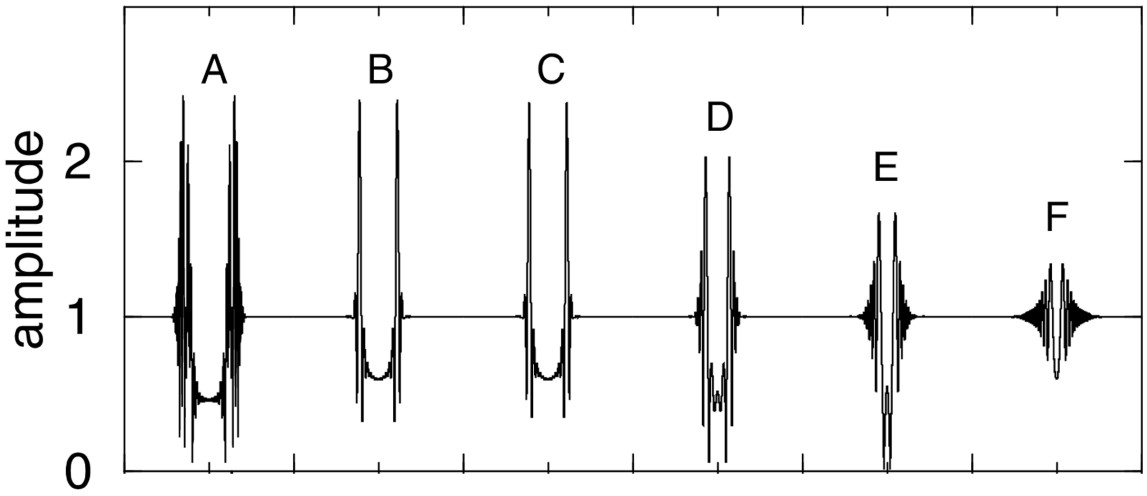

Figure 9. Series of phase screen simulations of GPS-frequency plane wave diffraction due to atmospheric plasma as run in Zeng and Sokolovskiy (2010). For plasma properties of each simulation (Table 1). Used with permission.

The distance between the plasma cloud and the final phase screen (the "receiver" in this simulation method) is 3000 km, the plasma profile in the z direction is a raised cosine (Zeng and Sokolovskiy, 2010), other parameters were varied as seen below.

Table 1. Plasma properties used by Zeng and Sokolovskiy (2010) to simulate diffraction patterns seen in Figure 9.

Simulation	Electron Density	Plasma Width (Δz)	Plasma Length (Δx)
A	$6 \times 10^5 \frac{e^-}{cm^3}$	100 km	4 km
B	$6 \times 10^5 \frac{e^-}{cm^3}$	50 km	4 km
C	$6 \times 10^5 \frac{e^-}{cm^3}$	100 km	4 km
D	$3 \times 10^5 \frac{e^-}{cm^3}$	50 km	2 km
E	$3 \times 10^5 \frac{e^-}{cm^3}$	52 km	1 km
F	$3 \times 10^5 \frac{e^-}{cm^3}$	10 km	0.5 km

If the current phase screen implementation can match these results it can be considered up to the standards necessary for further research. The results of performing

these simulations are seen in Figures 10-15. Note that all plots are rotated 90 degrees from Figure 9.

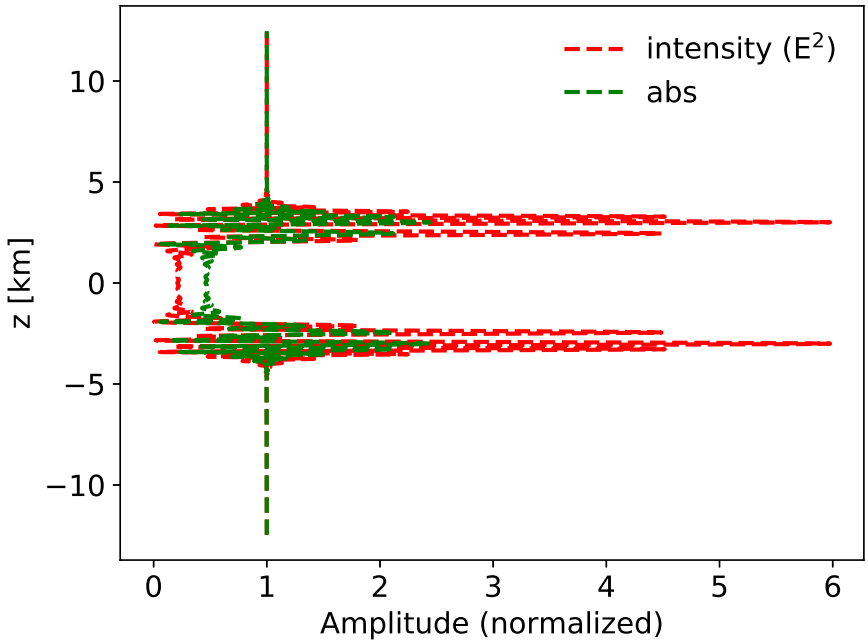

Figure 10. Reproduction of Zeng and Sokolovskiy (2010) simulation labeled A. Both the intensity of the simulated electric field (red dashed line) and the absolute value of the field (green dashed line) were plotted. The absolute field value matches Zeng and Sokolovskiy (2010) in both shape and magnitude, while intensity more explicitly shows the geometric features and is used in future S_4 calculations.

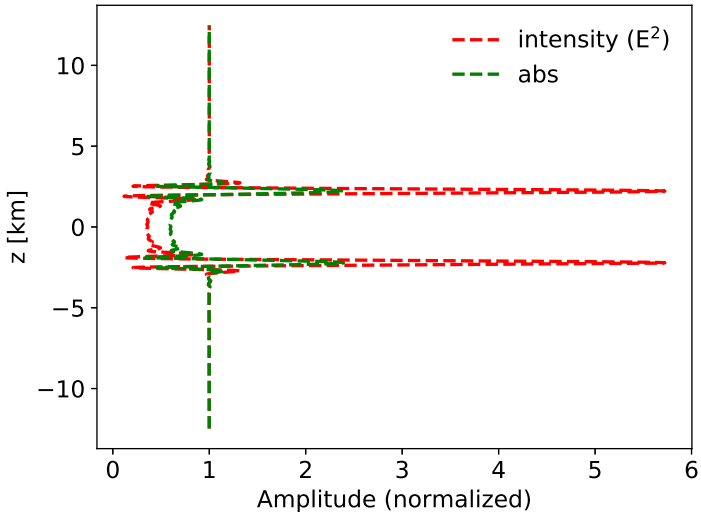

Figure 11. Reproduction of Zeng and Sokolovskiy (2010) simulation labeled B. Both the intensity of the simulated electric field (red dashed line) and the absolute value of the field (green dashed line) were plotted.

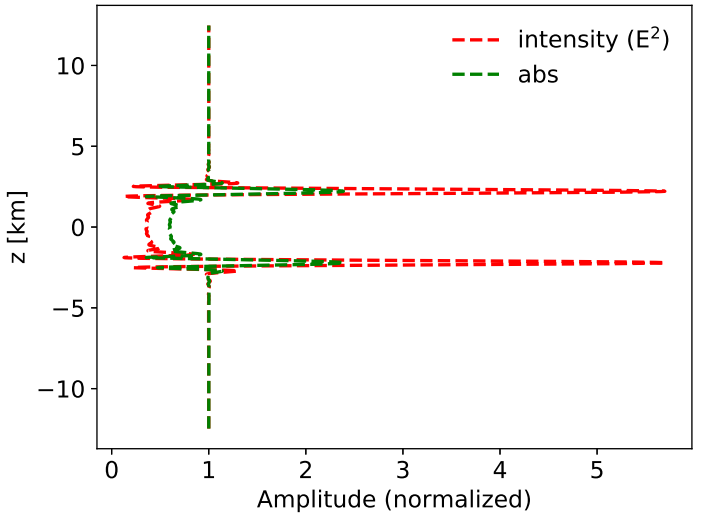

Figure 12. Reproduction of Zeng and Sokolovskiy (2010) simulation labeled C. Both the intensity of the simulated electric field (red dashed line) and the absolute value of the field (green dashed line) were plotted.

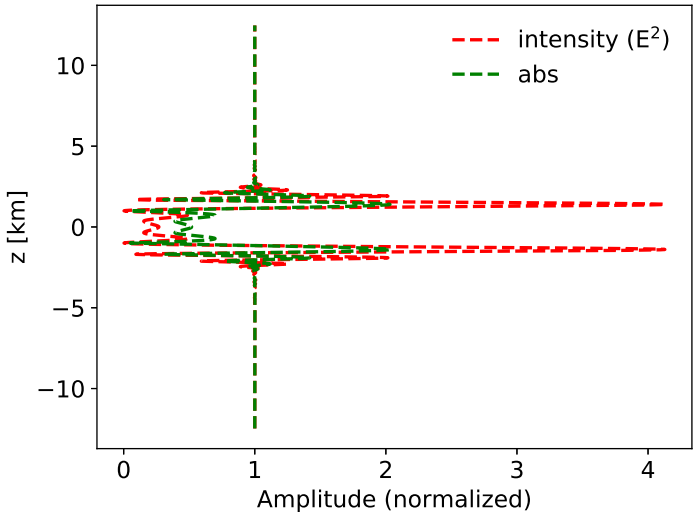

Figure 13. Reproduction of Zeng and Sokolovskiy (2010) simulation labeled D. Both the intensity of the simulated electric field (red dashed line) and the absolute value of the field (green dashed line) were plotted.

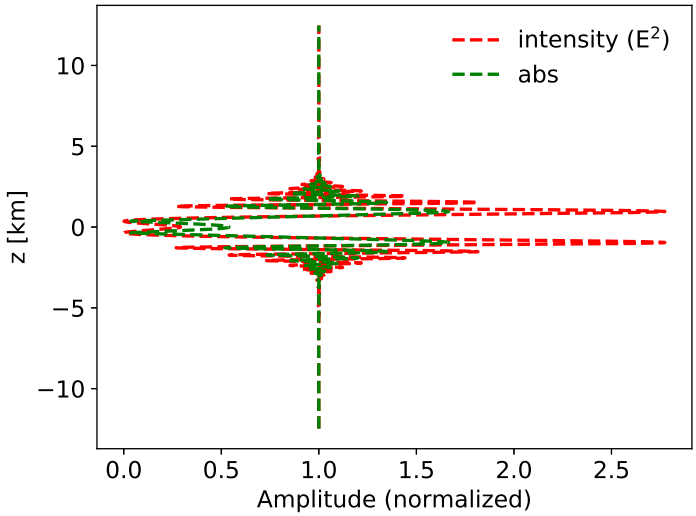

Figure 14. Reproduction of Zeng and Sokolovskiy (2010) simulation labeled E. Both the intensity of the simulated electric field (red dashed line) and the absolute value of the field (green dashed line) were plotted.

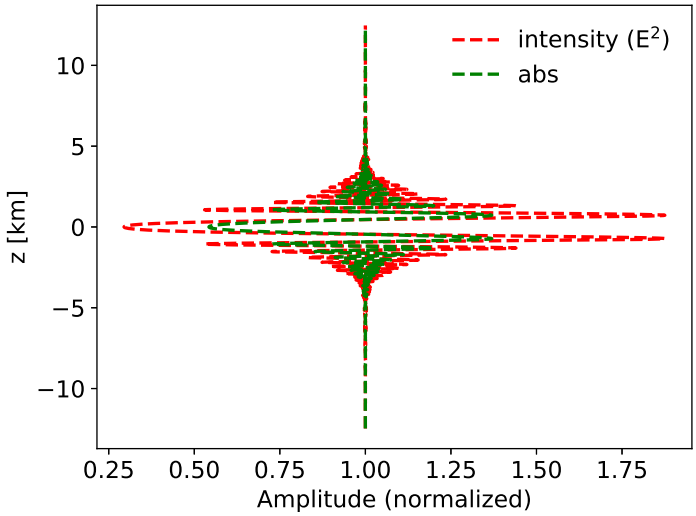

Figure 15. Reproduction of Zeng and Sokolovskiy (2010) simulation labeled F. Both the intensity of the simulated electric field (red dashed line) and the absolute value of the field (green dashed line) were plotted.

Overall Figures 10 through 15 show an outstanding match to the results by Zeng and Sokolovskiy (2010), validating the code and providing weight to future results.

3.3.2 Amplitude Variations

The simulations in this work are performed with the plane wave striking the plasma end on, that is perpendicular to the z profile of the sporadic-E cloud (Figure 16).

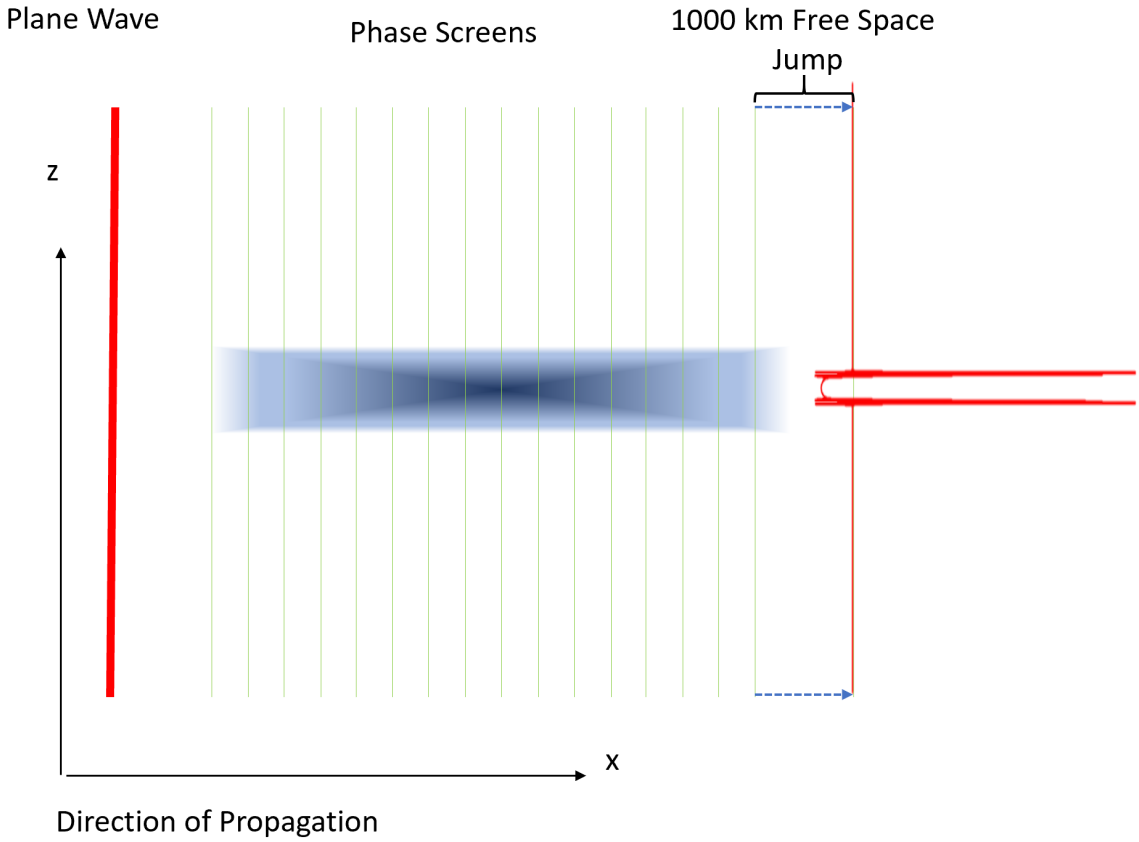

Figure 16. Overview of the simulation area showing orientation of RF planewave to plasma. The z direction is Representative of altitude and x of propagation distance.

Given this orientation, it is useful to ask how sensitive the simulation is to variance of the plasma in the x-direction. That is: are fluctuations in magnitude along x (random or otherwise) important to the the final intensity outcome? First it must be noted that plasma length and fbEs are tied in their effect on the simulation. What is important to the signal distortion is the optical path length, which includes both the physical distance and the index of refraction through which the RF is passing, so for a path s

$$OPL = \int_s n(s)ds. \tag{25}$$

This index is, in turn related to the plasma frequency and frequency of transmission

by:

$$n = \sqrt{1 - \frac{\omega_p^2}{\omega^2}} \tag{26}$$

for a plasma frequency ω_p and a signal frequency ω. Taking the Taylor approximation of for indices close to 1, as are seen for GPS signals in the atmospheric plasmas gives

$$n \approx 1 - \frac{\omega_p^2}{2\omega^2}. \tag{27}$$

If we look at the change in index from free space:

$$\delta n = \frac{\omega_p^2}{2\omega^2} \tag{28}$$

This means that a doubling in path length is equivalent to changing the fbEs by $\sqrt{2}$. Secondly it is useful to understand how a random fluctuation is added to the magnitude of the plasma affects the RF transmission. by multiplying each point by a random number between 0.75 and 1.00. The expectation is that the values will be integrated together and the total will act as a plasma with a slightly lower fbEs, although the exact effects are relatively minor (see Figure 19).

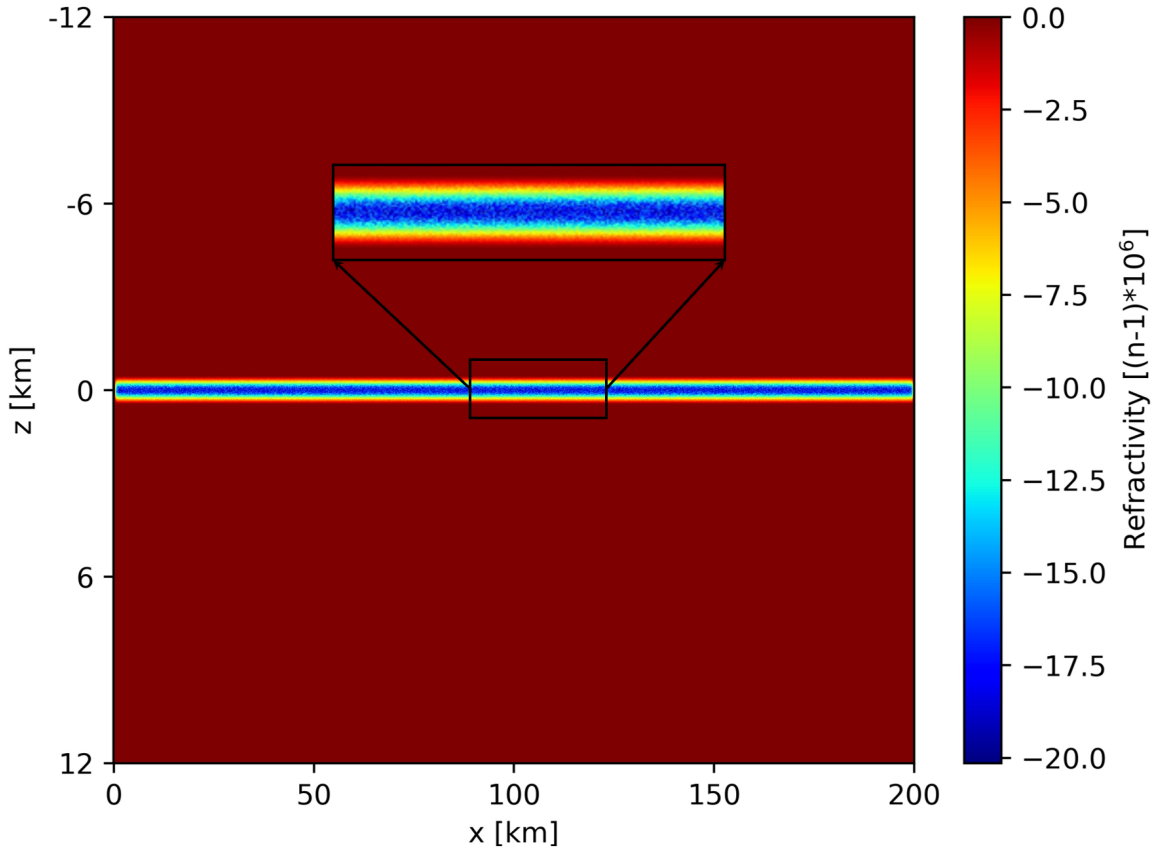

Figure 17. Plasma profile including fluctuations which lower the plasma intensity at each point by a random number between 0 and 25%. The zoomed in portion shows the speckles in the plasma density, fbEs before fluctuation is set to 10 MHz with a plasma width of 1km.

Instead, the rapidly shifting electron density values cause reflections into the $\pm z_{max}$ boundaries causing non-physical reflections (otherwise only seen for extremely strong plasmas) within the simulation. These reflections can be clearly seen in Figure 18.

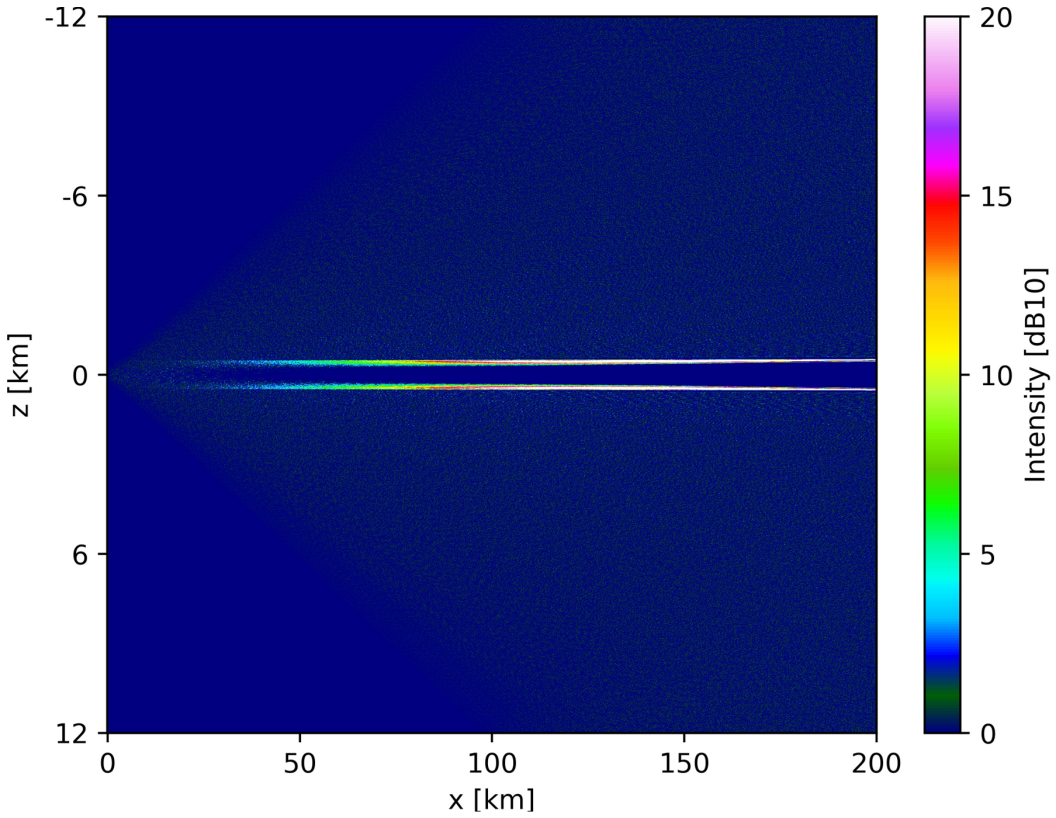

Figure 18. Field intensity in $10\times$dB to highlight the path deviations caused by relatively modest random fluctuations.

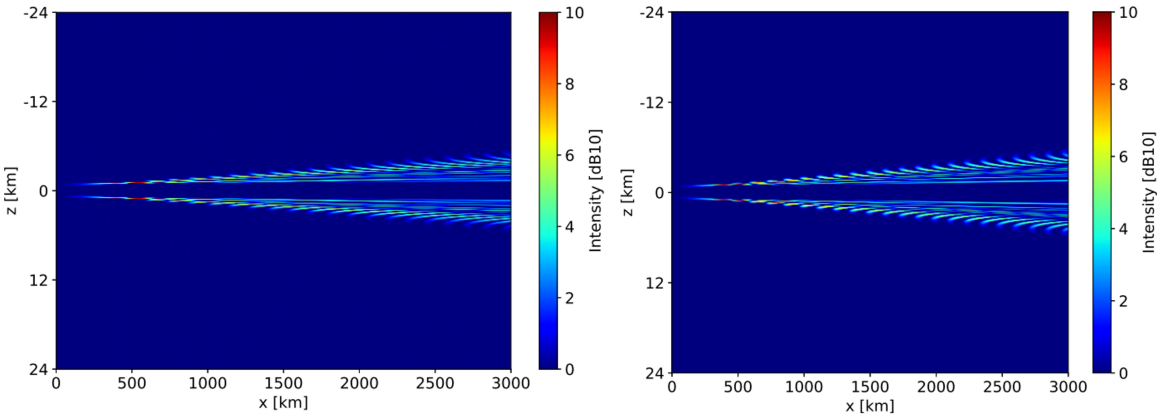

Figure 19. Although the reflections (amplified for visibility in Figure 18) do add noise to the final intensity, in practice as long as the fluctuations are kept to a minimum the effects will be small. These two plots are both of 5 MHz plasma, one with light (plasma intensity at each point is between 75% and 100% the non-fluctuated value) random fluctuations (left) and one without (right). The differences are somewhat difficult to make out, but the features in the simulation with random plasma fluctuations are less distinct than those seen more sharply on the right.

While these are not strong enough to derail the simulation completely (although they do add noise to the intensity plot, and change the final peak of the low-frequency plateau (see Section 3.3.4.1 below). How this changes the equivalent fbEs maximum, and what the noise does to the phase plots should be the focus of future work. This is the first indication that changes in index of refraction, rather than extremes of the value itself, are also of importance to the simulation outcome. This brings up an issue for the path length-fbEs relationship, however. The naive assumption that a change in fbEs can be swapped for a longer path length as calculated in Equations 25-28 must be tempered with one understanding that unless the difference in rate of plasma intensity change over that distance into account some error will be present as seen in Figures 20 and 21.

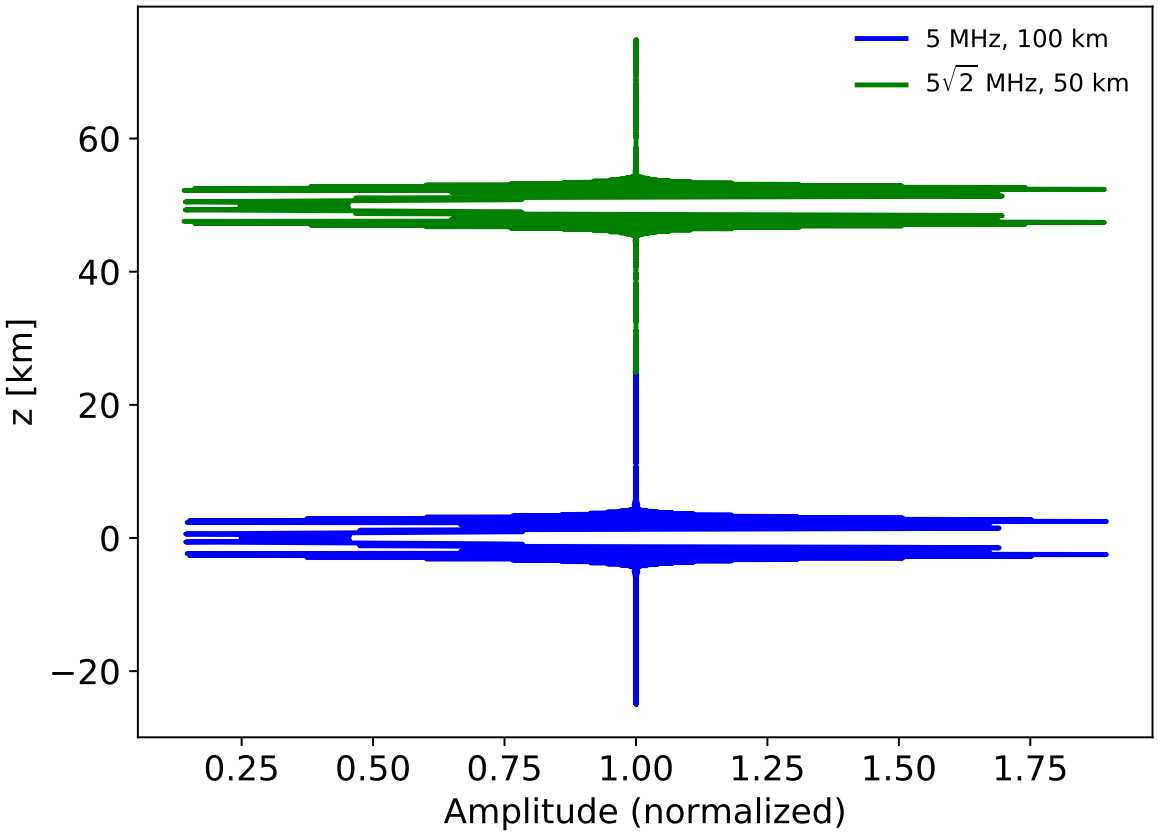

Figure 20. Intensity plots for a plasma with length 100 km at 5MHz fbEs (bottom) and 50 km with an fbEs of $5\sqrt{2}$ MHz (top). The error delta is most likely due to the different rates of change in the leading and trailing edges of the cloud.

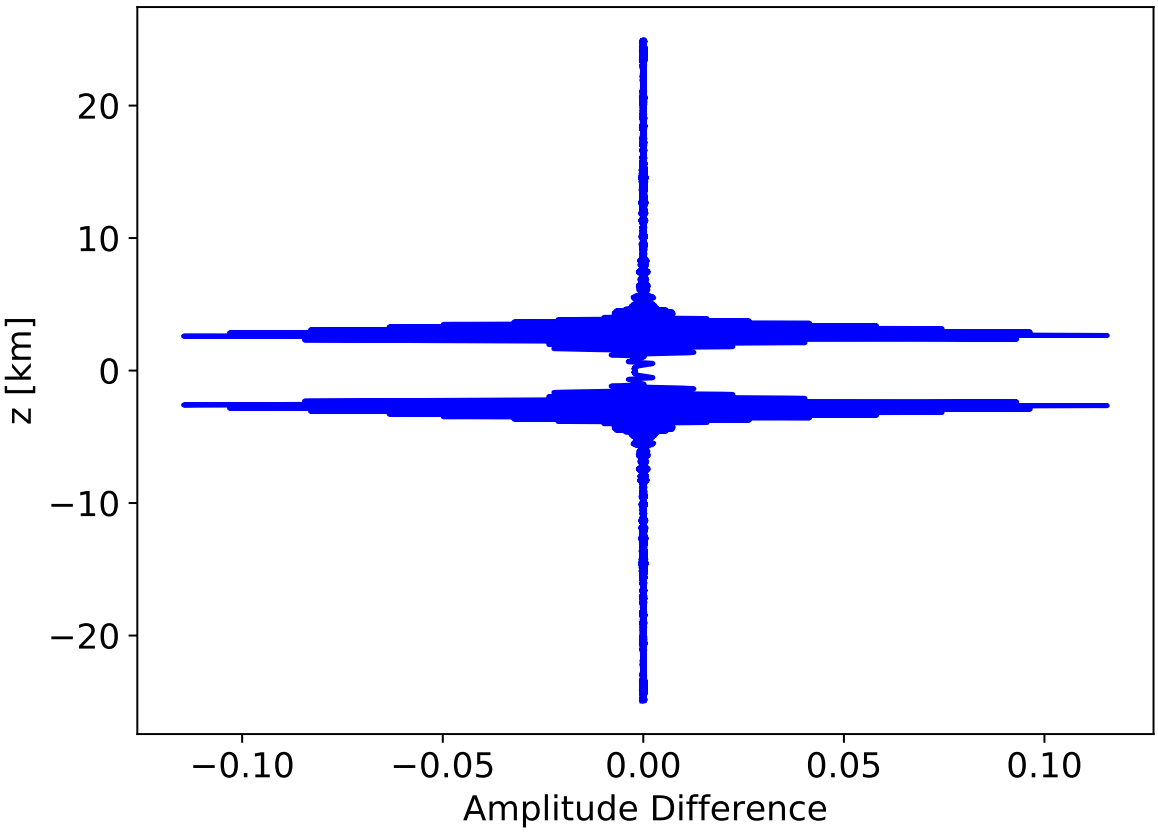

Figure 21. Intensity difference for plots in Figure 20, showing a small but not insignificant difference between the two simulations (the range is on the order of 10% of the intensity amplitude).

To drive home this conclusion the error between unaltered plasma and sinusoidally varying plasma with a profile with a complete wavelength of 350 phase screens corresponding to 35 km:

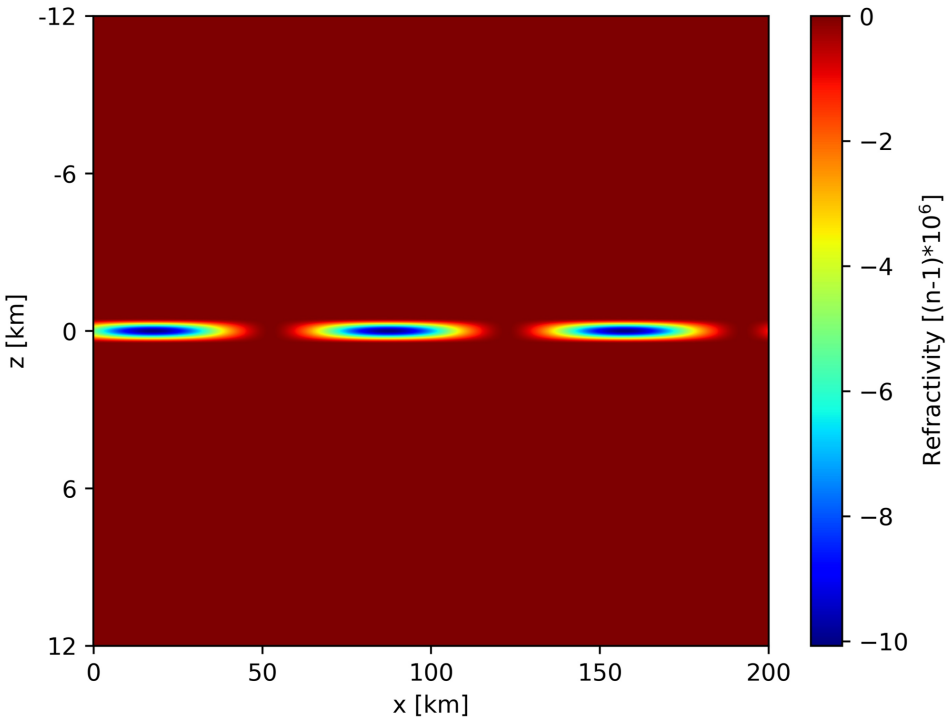

Figure 22. Sinusoidally varying plasma with a wavelength of 350 phase screens equivelent to 35 km.

This was compared to the error between unaltered plasma and a plasma with random attenuation between 0 and 25% as shown in Figure 23

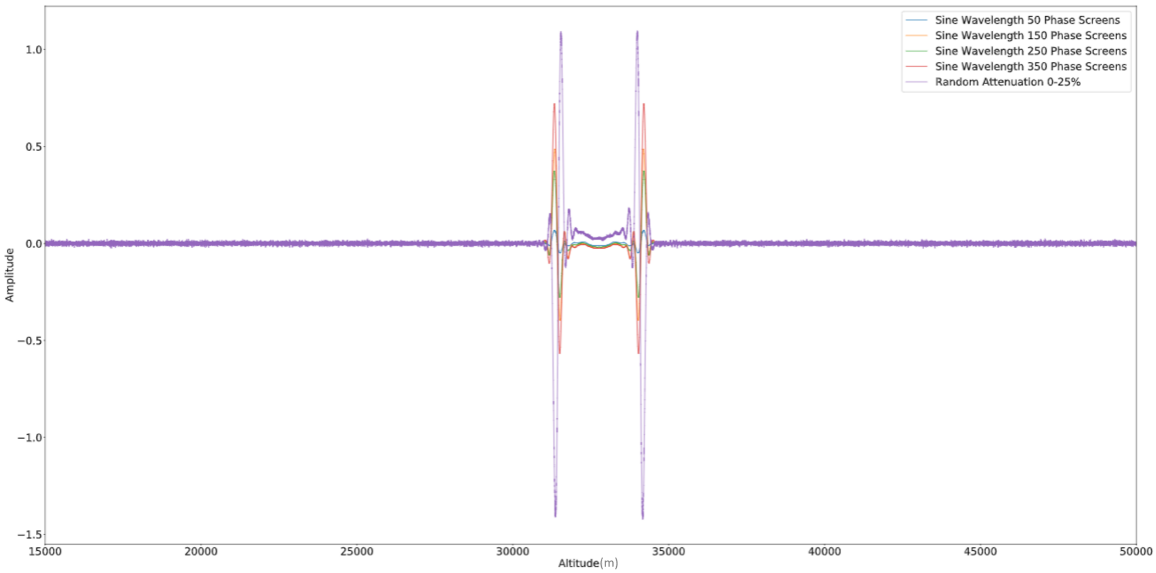

Figure 23. Amplitude plot of error curves (that is $I_{altered} - I_{unaltered}$) of the same plasma fbEs with an alteration in intensity either sinusoidal in x between fbEs$= 0$ MHz and fbEs$= 5$ MHz with a wavelength of 50, 150, 250, and 350 phase screens or a random attenuation at each point in x between 0 and 25%.

None the less, at least for these simplified sporadic-E simulations, the geometry is simple enough that sweeping simulations through both fbEs and plasma length would be redundant, and so will not be performed in the simulations below.

3.3.3 S_4 Simulations

Since S_4 is commonly used as a metric of sporadic-E strength and geometry, it is useful to provide an overview of the scintillation index. It is the normalized root mean squared deviation of the signal intensity (Beach et al., 2004) measured in these simulations as $I = |\vec{E}|^2$:

$$S_4 = \sqrt{\frac{\langle I^2 \rangle - \langle I \rangle^2}{\langle I \rangle^2}}. \tag{29}$$

In an effort to validate either the linear S_4 to fbEs relationship from Arras and Wickert (2018) or the competing theory of a potental non-linear relation from Gooch et al.

(2020), a series of simulations can be made sweeping through the fbEs parameter of a modeled sporadic-E to attempt to locate a linear region. The results in Figure 24

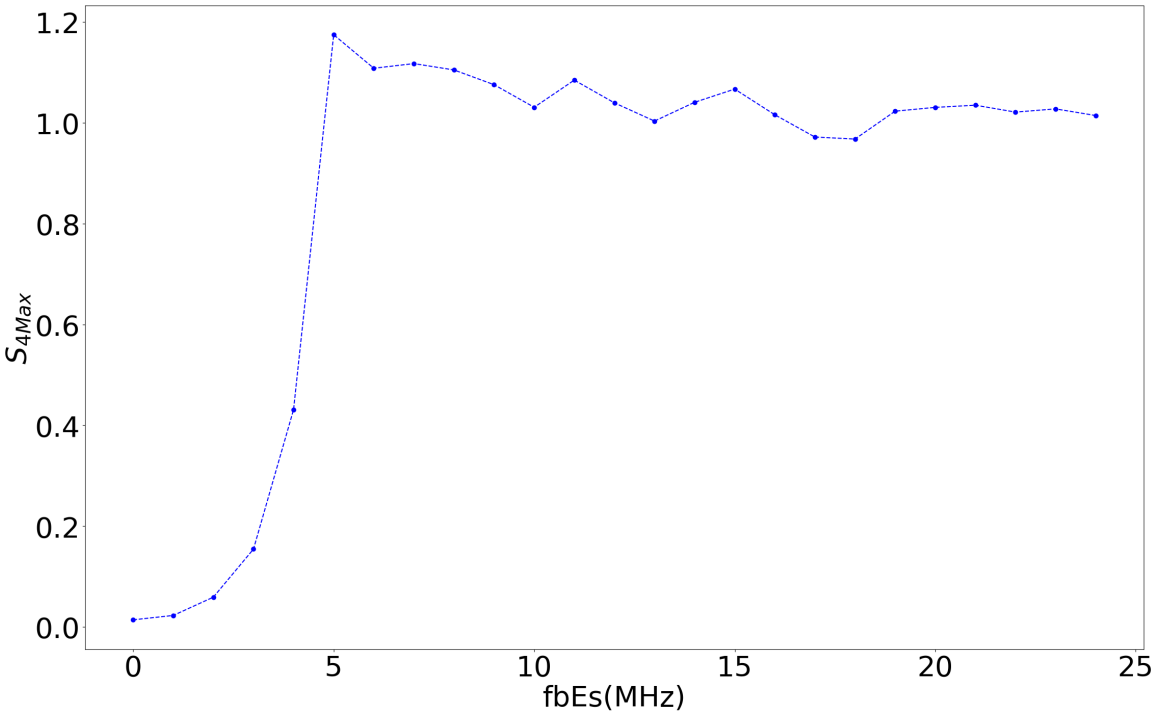

Figure 24. Maximum S_4 as a function of fbEs for a plasma cloud with a raised cosine profile with a width of 1 km and a length of 100 km, common sporadic-E values. The window of S_4 calculation was 100 m or three calculations per Fresnel radius, within the range suggested in Beach et al. (2004). The plot shows a distinctly non-linear relationship.

Clearly the S_4 to fbEs relationship is far more complex than the linear plot provided in Arras and Wickert (2018). That is not the only limitation of scintillation index, however, as is noted in Beach et al. (2004) S_4 neither characterizes phase fluctuations (also a problem for the spectral slope method described here) nor does it capture variations in index of refraction change as S_4 the saturation point of unity (Singleton, 1970). However, simulations using plasma strength/path length combinations which are physically possible in sporadic-E yield S_4 measurements above one. Even below this extreme, the precise point at which S_4 stops being useful for iono-

spheric characterization is unsettled: 0.5 (Hlubek, Nikolai et al., 2014) or 0.7 (Group, 2010) is considered high, and as discussed extensively in Singleton (1970), lensing effects (which are a common feature of sporadic-E RO) do not have the same electron density-to-S_4 relationship as random fluctuations in index of refraction. Further as Kamp et al. (2009) notes, the connection between scintillation index and total electron content (represented in the current work through fbEs values) starts to break down under strong scatter conditions with values of $S_4 > 0.25$. Finally the method in which S_4 is applied can dramatically affect the values of S_4 calculated. The scintillation index is calculated across a set of data points either from collected RO data as seen in Arras and Wickert (2018) or here simulated field intensity at each point in z. Utilizing the entire data set to calculate S_4, however, will include far too much non-diffracted data so a window of data points must be selected. It is the choice of window width, as well as the physical distance between points, that sets the granularity of the S_4 measurement, which in turn can cause variation in the calculated S_4 used to characterize the sporadic-E.

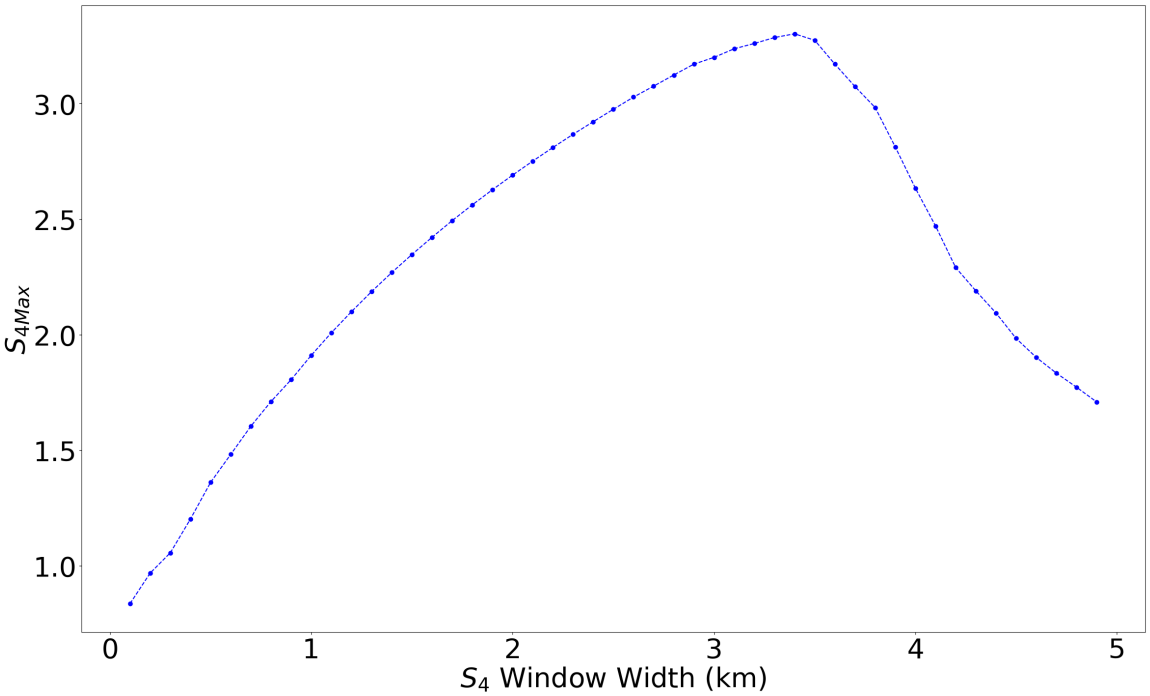

Figure 25. Maximum S_4 as a function of window width for a plasma cloud with a raised cosine profile with an altitude width of 1 km and a length of 100 km. The plot displays the importance of integration window to S_4 calculation. This is also a concern mentioned in Beach et al. (2004). The peak in window size is a result of the comparative size of the window width and the high frequency regions on the edges of the peculiar U-shaped disturbance, examples of which are seen in Figures 10-15, characteristic of sporadic-E RO.

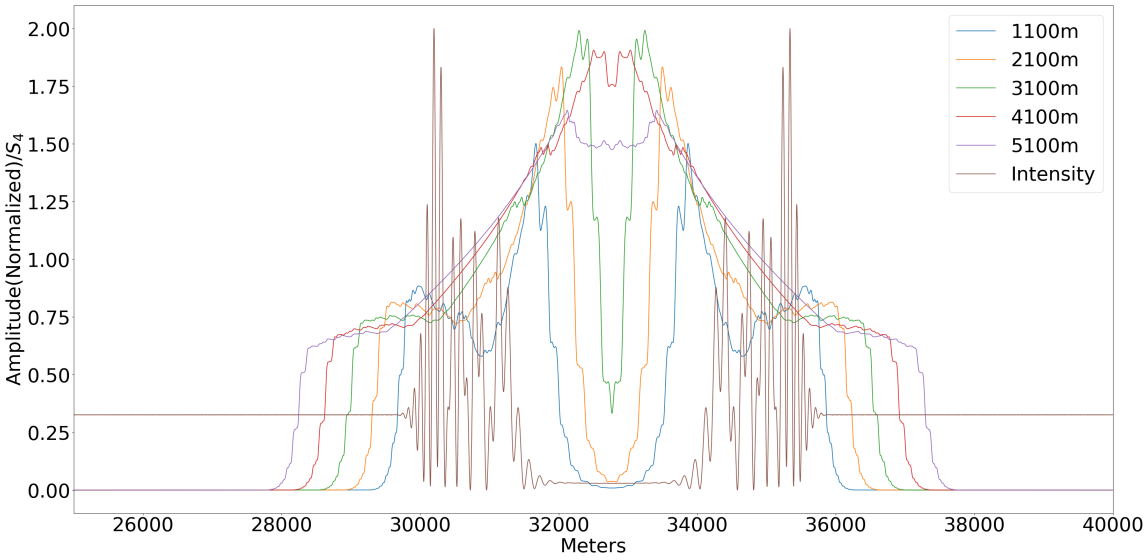

Figure 26. Superimposed plots of a series of S_4 plots with varying window widths as well as an intensity plot normalized to 2. This allows a visual comparison of how the window across which S_4 is calculated compares to the features in the intensity plot and why S_4 values peak at approximately 3 km. A window this size is large enough to encompass a high variance, while having the average (the denominator in the S_4 calculation) be pulled down by the central portion of the U-shape. This results in an extraordinarily high maximum S_4 measurement.

Even simplifying S_4 to a standard deviation retains this windowing issue, plotting

$$\sigma = \sqrt{\langle I^2 \rangle - \langle I \rangle^2} \tag{30}$$

for a set of window sizes yields the series of traces in Figure 27:

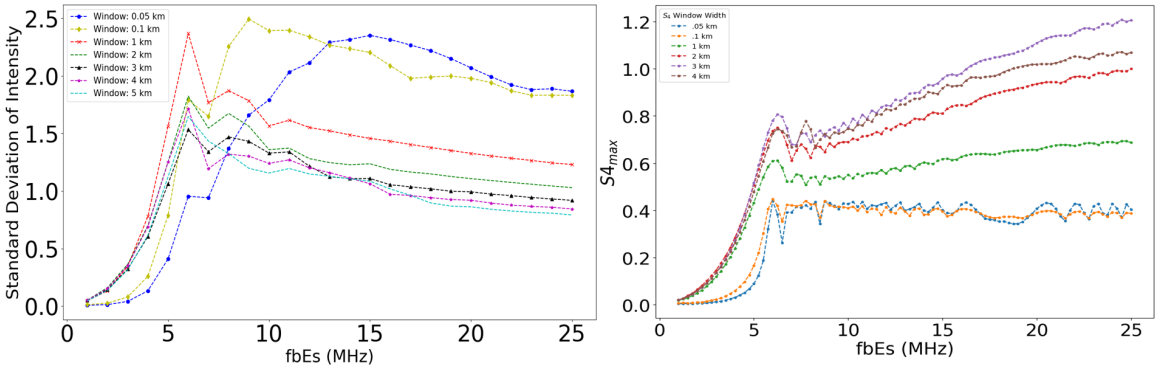

Figure 27. Comparison of shifts in standard deviation (left) and S_4 (right)of the same sweep of fbEs values with different window sizes. While the behavior remains fairly constant with exponential increase followed by sinusoidal variation the values vary between data sets.

While there is a place for S_4 in sporadic-E research, the variability seen here highlights the need for another supplementary metric if RO is to be used to characterize the plasma.

3.3.4 Spectral Analysis Methods

In order to build a metric that will provide a reliable mechanism of classifying sporadic-E RO signals, we start by taking the spatial Fourier transform of the final output screen of the phase screen simulation. Figures 28 through 31 include a plasma of length 100 km and width 1 km.

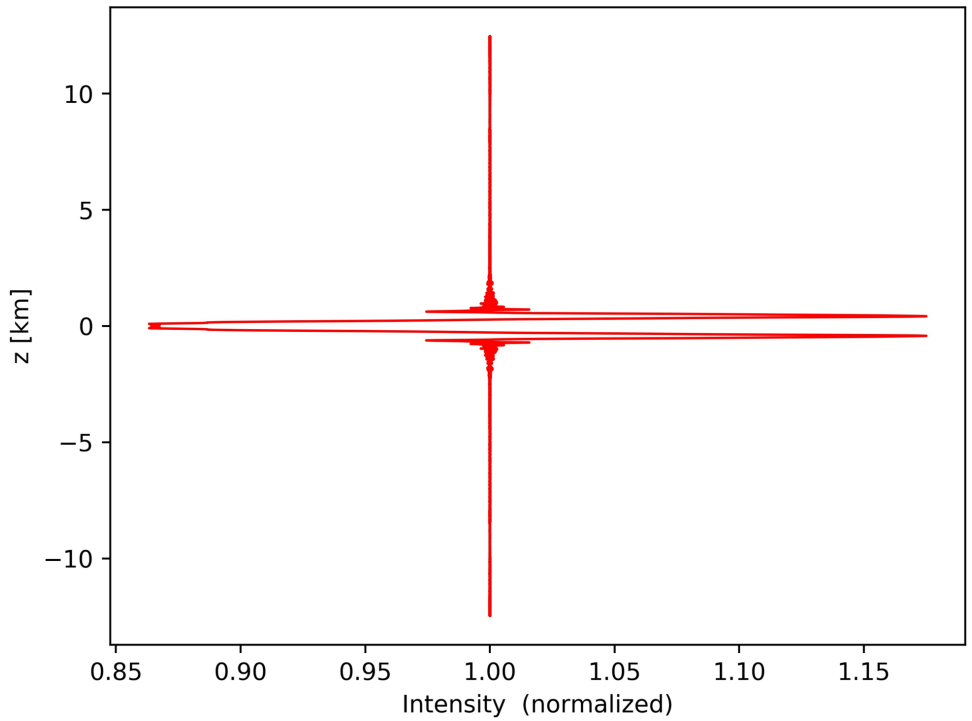

Figure 28. Simulated RO E^2 intensity vs altitude plot showing the effect of a plasma cloud with a 2 MHz blanketing frequency on a GPS L1 frequency plane wave.

The Fourier transform of this can be taken using the standard Fast Fourier Transform algorithm in Python's "numpy" package with a sampling frequency of $\frac{1}{dz}$. Figure 29 reveals the spatial spectral content of the diffracted planewave.

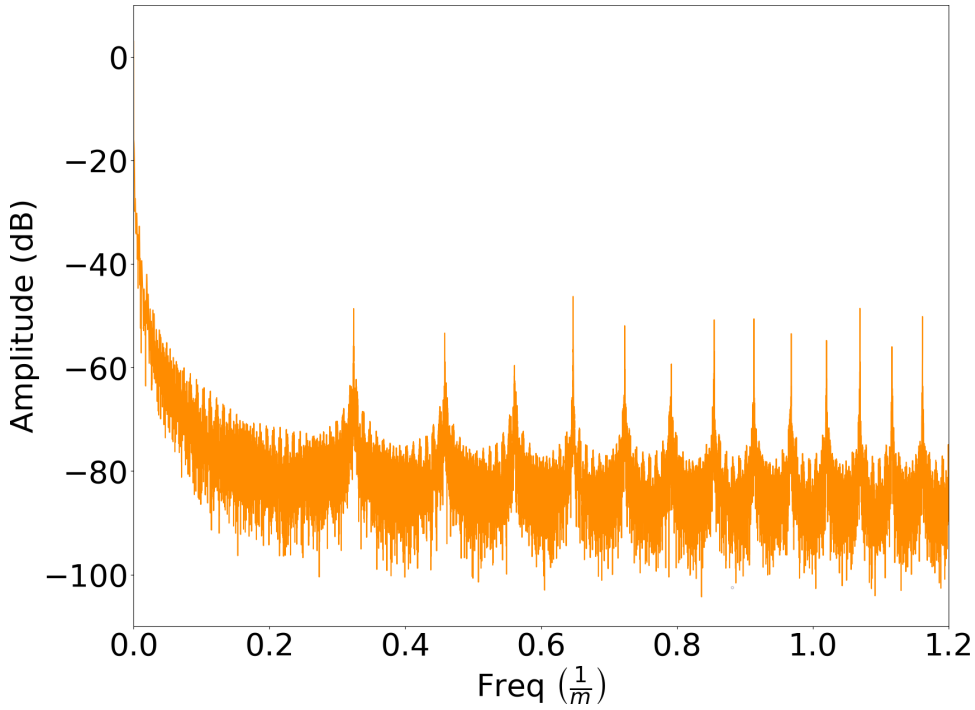

Figure 29. Fourier transform of simulated RO intensity vs altitude showing the effect of a plasma cloud with a 1 MHz blanketing frequency on a GPS L1 frequency plane wave.

These plots can be compared to Figures 30 and 31 to see how increased fbEs correlates to alterations in the spatial frequency content.

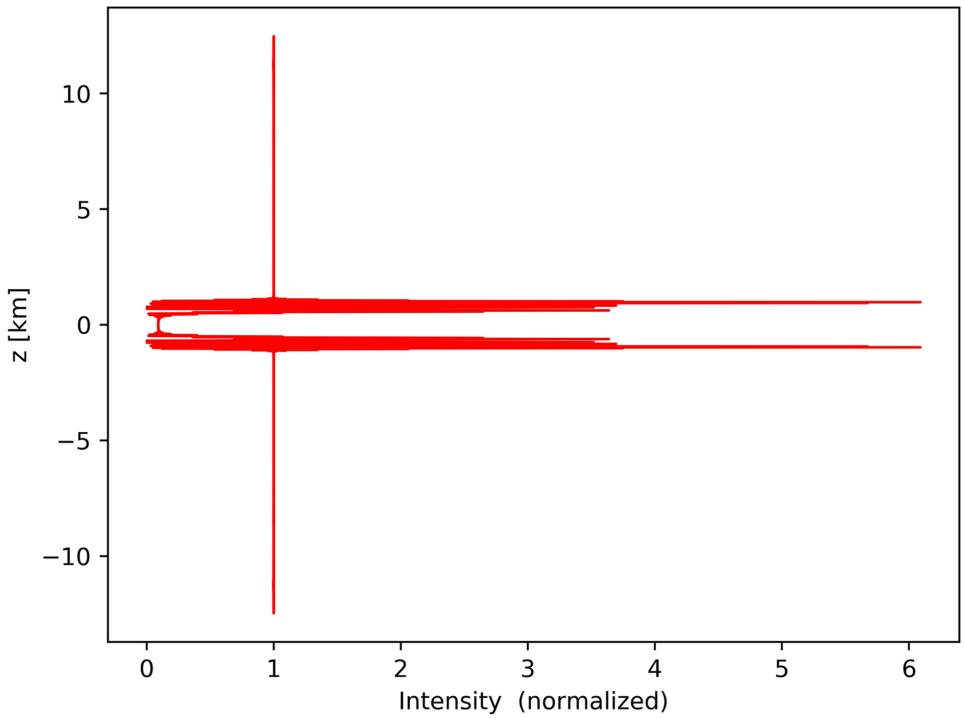

Figure 30. Simulated RO intensity vs altitude plot showing the effect of a plasma cloud with a 10 MHz blanketing frequency on a GPS L1 frequency plane wave.

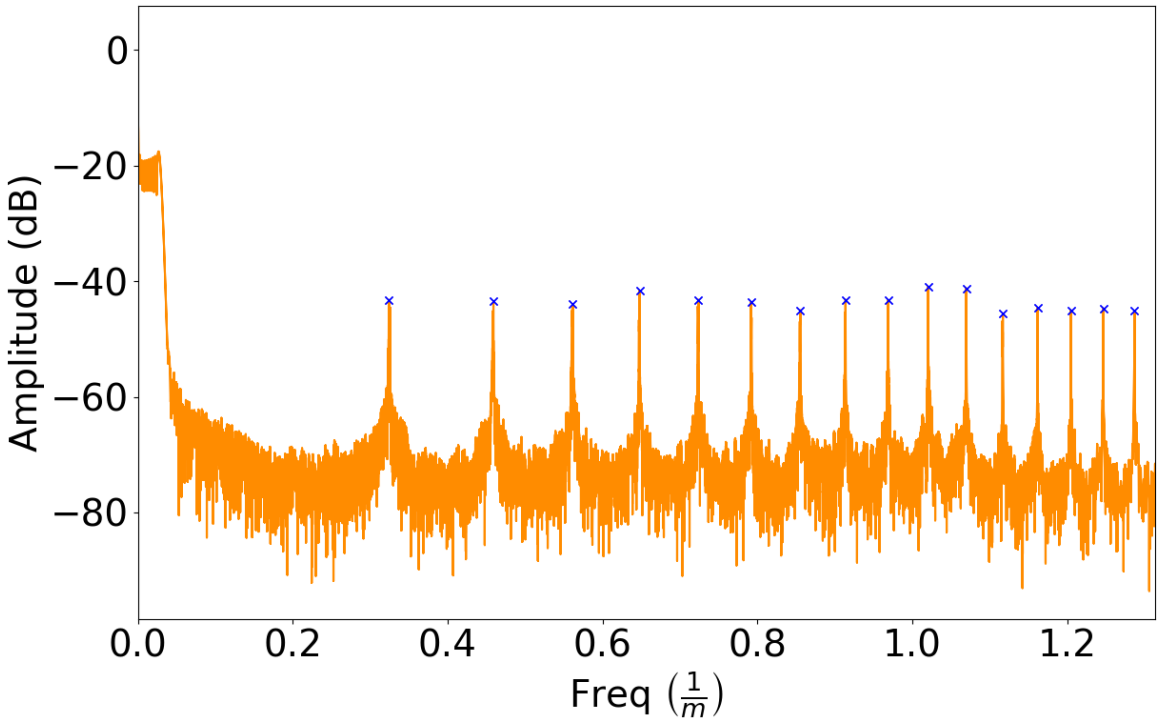

Figure 31. Fourier transform of simulated RO intensity vs altitude plot showing the effect of a plasma cloud with a 10 MHz blanketing frequency on a GPS L1 frequency plane wave.

There are two major differences that can be observed between the two Fourier transforms: the low-frequency plateau and the higher frequency spikes. While it may be tempting to use the high-frequency spikes as an identifying fingerprint of plasma properties, their low amplitude makes them quickly fall below the noise level under non-ideal cases. Adding random noise level between 0 and ±1% to the initial plane wave amplitude raises the noise floor sufficiently to mask the identifying spikes (Figure 32).

3.3.4.1 Plateau Endpoint

This leaves the low frequency plateau from which to extract identifying metrics. The formation of the plateau correlates with the generation of the classic u-shape seen

in sporadic-E RO (see Knepp (1982), Zeng and Sokolovskiy (2010) for examples). Here we focus on two characteristics of the transform plot: the frequency of the final peak of the plateau, and the slope of the fall-off. The first of these is fairly self explanatory (although there is a quirk discussed below) and is readily apparent in Figure 33 where it is highlighted by the red vertical line.

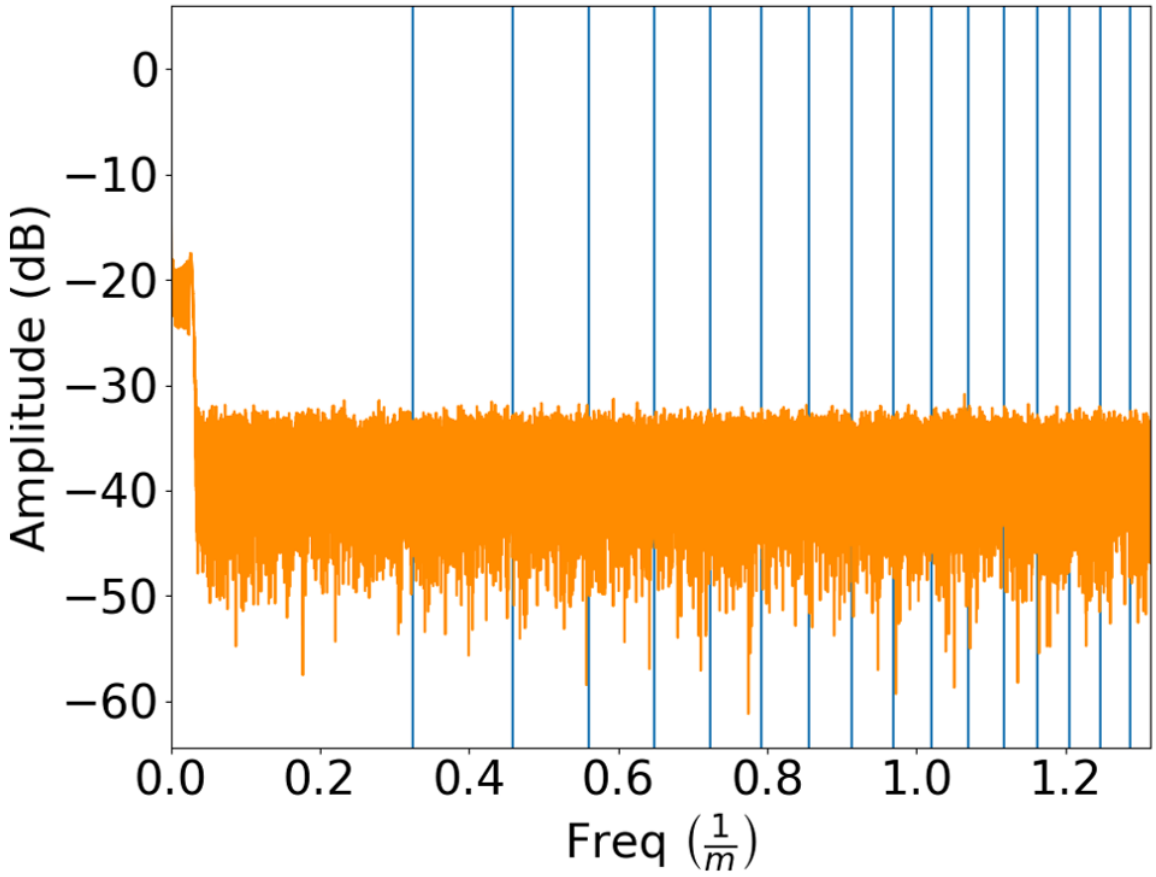

Figure 32. Fourier transform of simulated RO intensity vs altitude under the same conditions as Figure 31 with a random amplitude adjustment between 0 and ±1% added to the planewave at each point in z upon generation at the start of the simulation. The blue bars indicate the frequency location of the peaks highlighted by an 'x' in Figure 31. The increased noise floor clearly makes identifying these peaks without foreknowledge impossible.

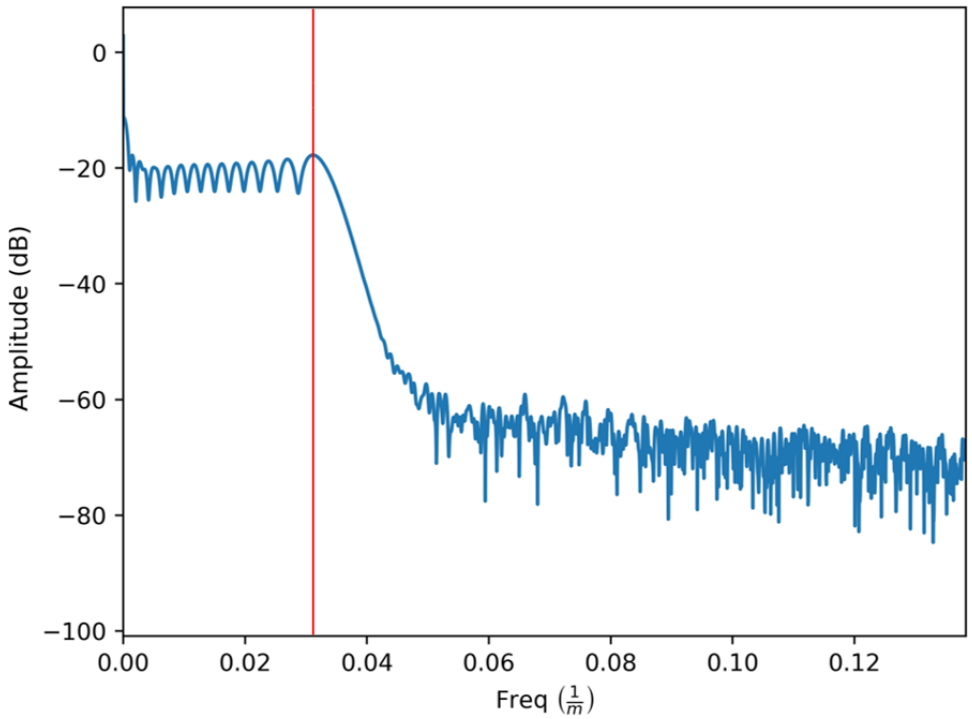

Figure 33. Zoomed in view of Fourier transform of simulated RO intensity vs altitude under the same conditions as Figure 32 inclusive of the added noise. The red bar indicates the location of the final peak of the low frequency plateau before drop-off to the noise floor.

The location of this point shifts with the intensity of the disturbance of the planewave as it propagates through the simulated sporadic-E, and is at most only mildly disturbed by all but the most extreme noise levels.

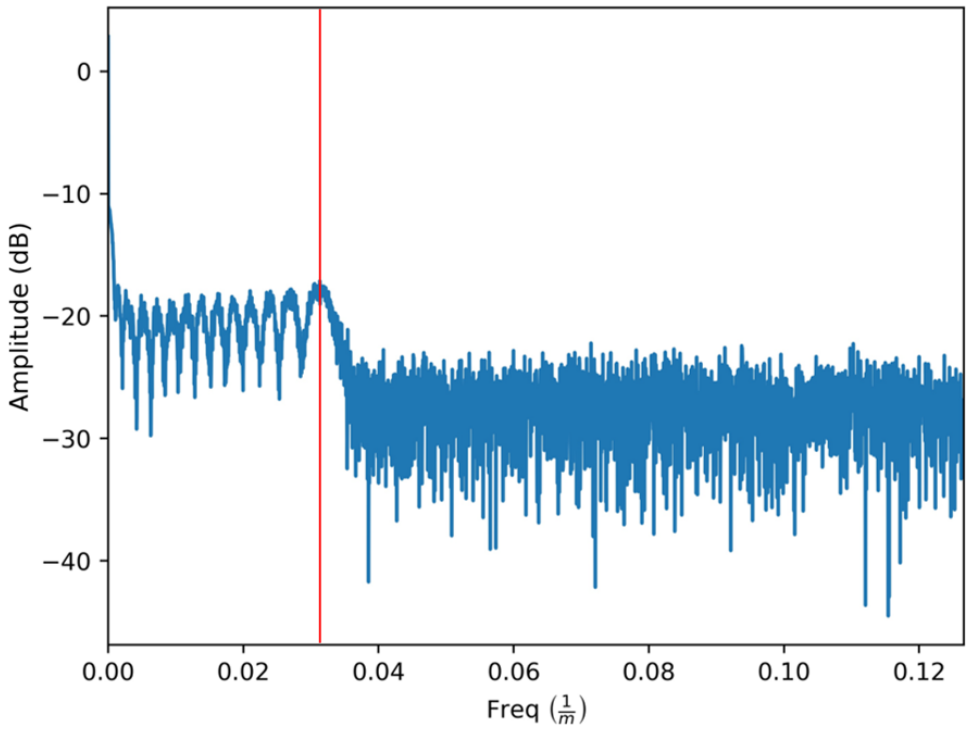

Figure 34. Zoomed in view of Fourier transform of simulated RO intensity vs altitude under the same conditions as Figure 32 with a random amplitude adjustment between 0 and ±50%. While the noise floor has risen dramatically, the ability to still easily pick out the relevant peak speaks to the resilience of this method.

The downside of this method is at lower levels of wave diffraction the plateau has not had a chance to form (a phenomenon which first appeared between 2 and 2.5 MHz for a plasma 100 km long and 1 km wide), this can be seen in Figure 29. Rino (2011) suggests this pre-plateau region correlates with weak scatter and the formation of the plateau is the transition into the strong scatter regime.

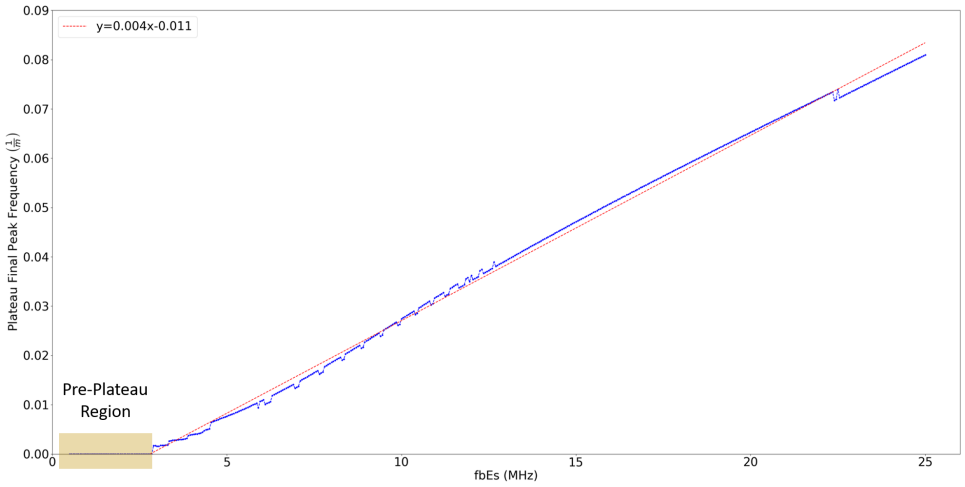

Figure 35. Plot of frequency of final peak as a function of fbEs, note the pre-plateau region extends to a blanketing frequency of 2.75 MHz for a sporadic-E length of 100 km and a width of 1 km. Both of these parameters will affect the fbEs frequency at which the plateau will form. Once the plateau forms the final peak frequency increases fairly linearly with the fit line given.

Clearly Figure 35 gives a clear linear relation relationship between the final peak frequency and the fbEs value and this gives a classification mechanism for the sporadic-E once the scattering on the GPS signal has reached the level where the plateau forms. Plotting the final peak frequency against plasma width (Δz) yields a contrasting result.

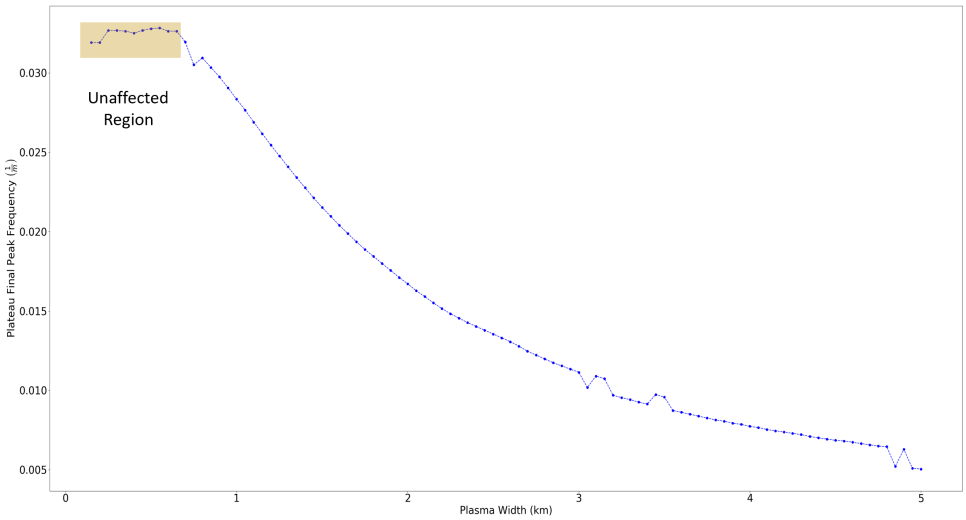

Figure 36. Plot of frequency of final peak as a function of plasma width (Δz). At widths below 0.5 km alterations in plasma width seem to have minimal effect on the width of the plateau, once that point has been passed the width decays exponentially. Note that fbEs for all simulations is 10 MHz.

The dramatic fall off in the width of the low-frequency plateau comes despite the maximum plasma frequency remaining unchanged; in fact there is a greater area covered by the high-intensity plasma at the larger values of Δz. A comparison of the refractivity ($(n-1)*10^6$ for an index of refraction n) between the widest and narrowest plasma profiles can be seen in Figure 37.

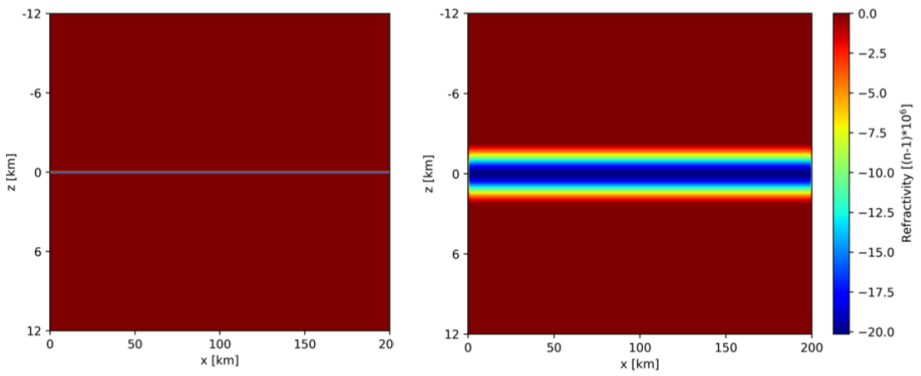

Figure 37. Comparison of the plasma geometries on either extreme of the set of simulations plotted in Figure 36. Note that the maximum refractivity is the same on both and the cross-section on each is a raised cosine described by the Hanning window.

These profiles resulted in the intensity profiles displayed in Figure 38.

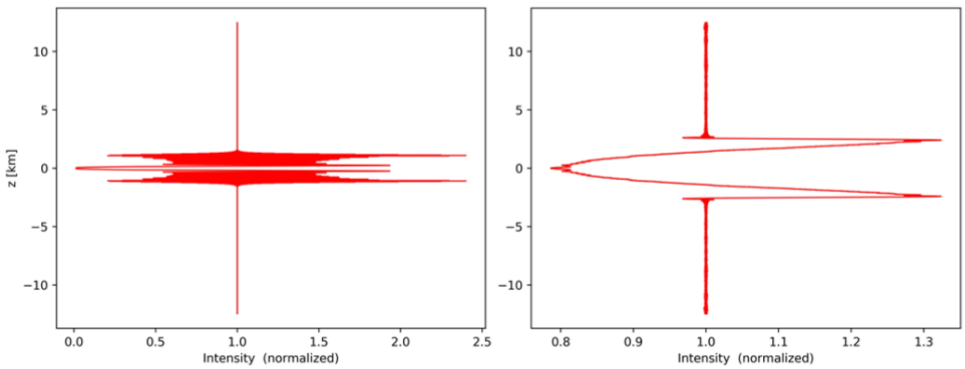

Figure 38. Intensity (E^2) profile for plasma width of 0.5 km (left) and 5 km (right) correlating to Figure 37. Note the amount of diffraction that occurs on either edge of u-shaped central depression. The wide plasma profile on the right causes a wide area of attenuation with much less diffraction.

These results support the intuition that the diffraction patterns on the edge of the u-shaped depression include high-frequency components that extend the width of the plateau. The final maximum of the plateau as plotted in Figure 36 is closely tied to the rate at which the index of refraction of the changes. The connection between rate of index variation and signal distortion has been noted in other works on sporadic-E effects (Wu et al., 2005) on received GPS signal-to-noise (SNR) and phase values. Using the final peak of the low-frequency plateau seems to be a fairly robust metric within certain bounds. It is useful as long as the transmitted wave has encountered enough distortion for a plateau to form. Once it has, it gives an insight into the plasma strength as well as vertical cross section of the plasma beyond simple maximum blanketing frequency. As can be seen in the plasma profiles documented by the Arecibo Observatory and presented in Figure 2, the rate of electron density change in sporadic-E layers can change wildly with height. Thus this metric may well provide some insight into the smaller-scale structure of the sporadic-E, although more exacting simulations and measurement comparisons will be needed.

3.3.4.2 Spectral Slope

A second metric is the rate of fall-off from the point of the final peak to the noise floor. This method was explored in Carrano et al. (2011) where Fourier transforms similar to what is seen in Figure 33 are plotted in a log-log scale to produce a linear region correlating to this fall-off. The slope of this area (see Figure 39) is the exponent x in the 10^x fall off. This method of determining the slope can be applied to the fall off from the low-frequency plateau to give a second metric with which to analyze the sporadic-E. To apply this metric a series of sporadic-E variable sweeps was performed and the magnitude of this value compared.

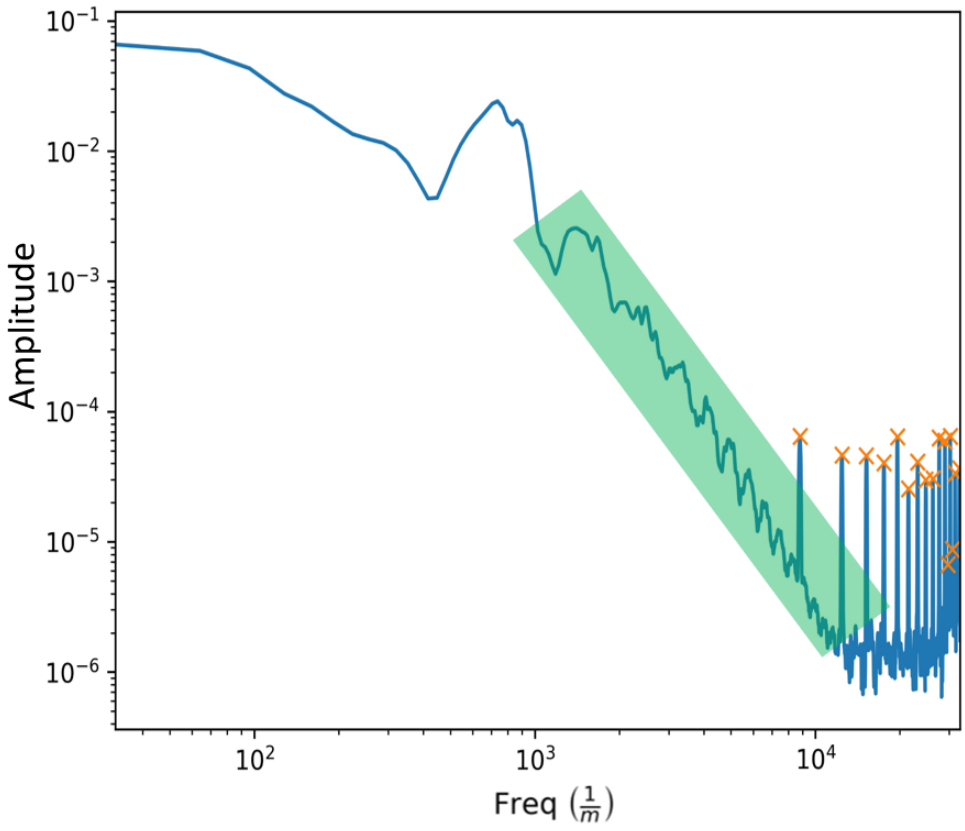

Figure 39. Sample of a log-log plot of the FFT of the final intensity showing the spectral slope. The linearity of the slope is an artifact of the logarithmic plot, and is actually a base 10 exponent.

In order to determine this slope, a low and high frequency point must be selected. The low frequency point is the final peak from the plateau as utilized in section 3.1.2.2 above. The second point should ideally be where the noise floor begins, although actually determining a single point can be challenging. To find this point, first a Savitzky-Golay filter (see Schafer (2011) for an in depth review of this form of noise reduction) is applied to the Fourier transformed intensity to reduce the random noise on the floor. The derivative is taken to find the point at which the noise floor flattens and that becomes the high-frequency point of the slope. An example of this is shown in Figure 40.

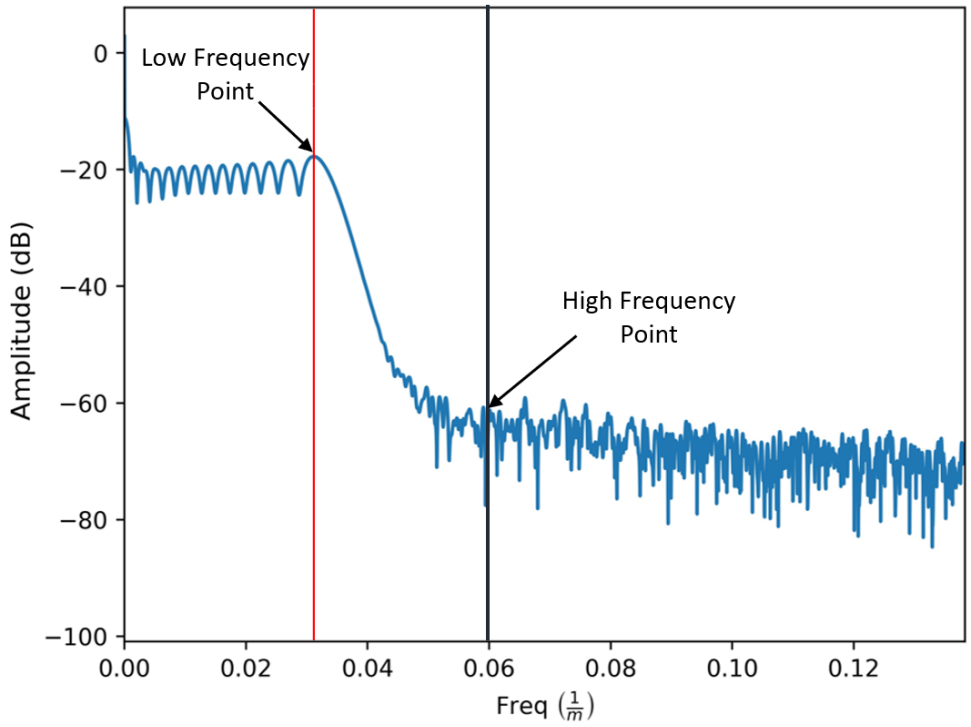

Figure 40. An example of the selection of high and low-frequency points for slope calculation with $\Delta z = 1$ km, $\Delta x = 100$ km, and fbEs $= 11.7$ MHz. The high-frequency point, marked with the red vertical line, is at selected at the point where the average of the derivative of the FFT, designated by the blue trace, is 0 following it's absolute minimum.

Note that the high-frequency point remains within the noise floor which causes some

variability, an average is taken in an area ±40 points around the selected point, however it is still a major cause of variability. The Spectral Slope between these points is the exponent of the decay between these two points (all the Fourier transform plots are in dB) and can be taken for a large series of simulations while varying the three main sporadic-E plasma parameters. The first of these is blanking frequency and is plotted below in Figure 41.

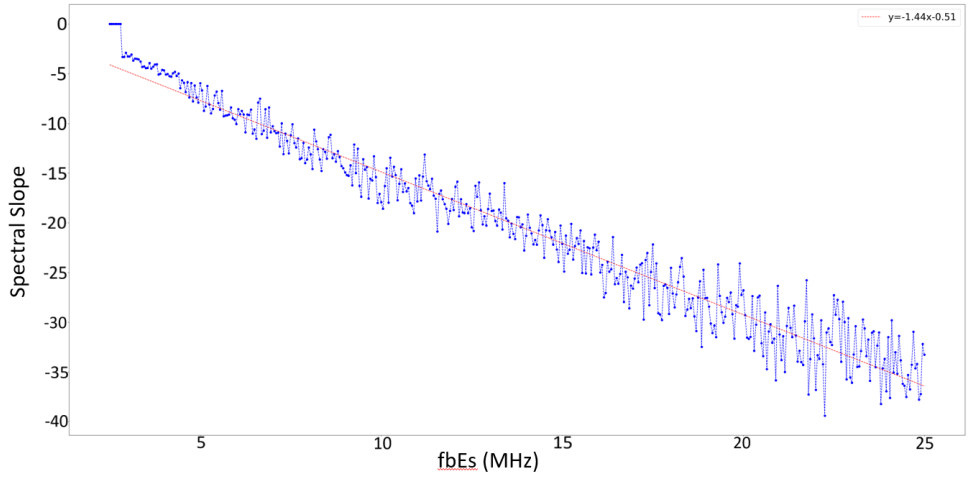

Figure 41. Calculated spectral slope vs fbEs displaying the linear relationship between the two when other plasma parameters are held constant ($\Delta z = 1$ km, $\Delta x = 100$ km). The variability is due to the difficulty of selecting a precise point within the noise floor, as mentioned above.

The clear relationship between spectral slope and fbEs shows the promise of the metric. It is a result which makes good the intuitive sense that increased scintillation produces more higher frequency content (as it did with the expanding low-frequency plateau) and thus the fall-off from the plateau should be slower. The linearity of the result does give a good indication that the spectral slope may be used to produce a look-up table, although the sensitivity to noise may make it less resilient of a metric than the width of the low-frequency plateau. The same series of calculations was performed on a set of simulations of varying plasma widths (Δz) with the same

values in Figure 36 and the data in Figure 42 was produced.

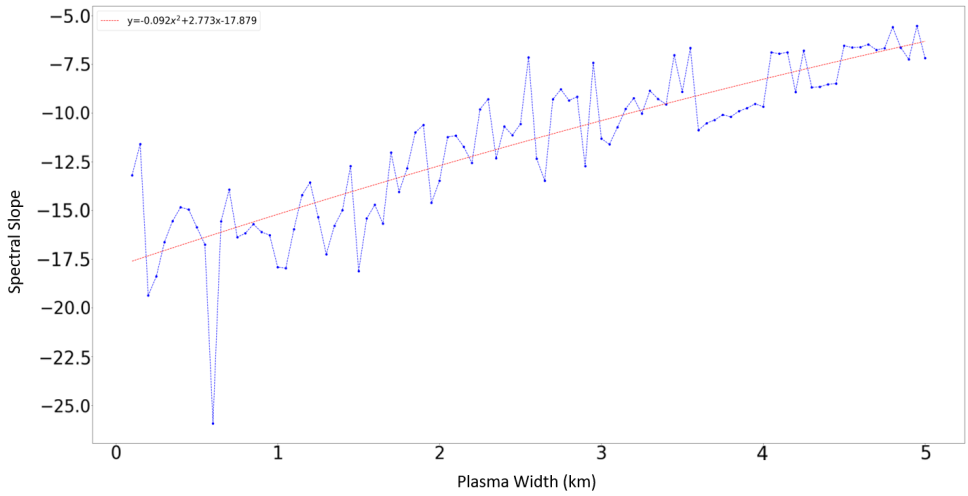

Figure 42. Calculated spectral slope vs plasma width. Although fairly noisy a clear trend is emerges of parabolic decrease in signal disruption with increasing plasma width (fbEs is maintained at 10 MHz and plasma width at 100 km). Again this is probably attributable to the slower variance in plasma that occurs as the Hanning layer is stretched out while maintaining the same maximum fbEs value.

Again a trend appears, this time a quadratic fall off of the spectral slope magnitude (if the Δz is pushed much farther the low-frequency plateau collapses all together and the slope falls off quickly). This matches the drop observed of the final peak of the low-frequency plateau seen in Figure 36 and probably for the same reasons. Again the noise values are a potential cause of trouble, and the applicability of this method to a noisy environment is questionable.

3.3.4.3 Disentangling Plasma Length

As mentioned above, for the previous simulations the plasma length was held mostly constant while the fbEs value was varied. This is is because the net effect of the sporadic-E on the plane wave passing through the plasma accumulates over the span of the plasma. This means that any metric used will not uniquely identify a

specific fbEs or plasma length, but rather a combination of the two. In an attempt to find a way of deconvolving these two sporadic-E characteristics the simulations plotted in Figure 43 were run.

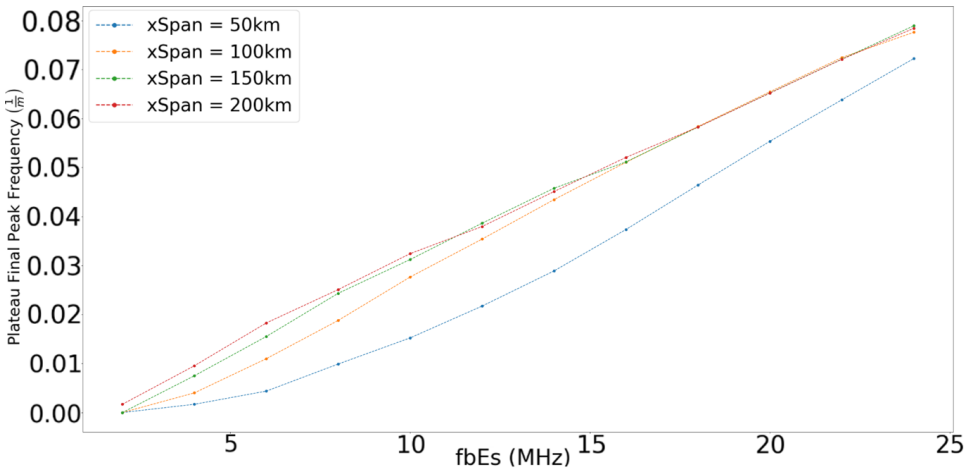

Figure 43. A series of simulation runs showing the change in final plateau frequency across varying fbEs for four different plasma lengths.

As can be seen the plots do in fact differentiate themselves, and point at a possible means of identifying plasma length (labeled as xSpan in the plot) separately from fbEs. A RO measurement that utilizes a frequency sweep (thus varying the ratio of signal frequency to plasma frequency) could possibly be used to identify a specific slope correlated with a plasma length, and thus both factors could be identified. Unfortunately no such data currently exists, however this result does suggest a development path for future RO hardware.

IV. Conclusions

This study analyzed the performance of multiple phase screen simulation techniques of GPS radio occultation applied to an idealized sporadic-E geometry. This simulations set was designed to test the applicability of the S_4 metric previously utilized to determine key characteristics of the sporadic-E cloud. The applied simulations cast doubt on the breadth of applicability of S_4 as attempts to reproduce the linear relationship between S_4 and plasma properties instead yielded nonlinear relationships which rapidly approached unity, something not seen in measured scintillation data. The current work presents some promising alternatives to fill the metric gap. Through phase screen simulations of geometrically simplified ionospheric disturbances, and their effects on GPS L1 frequency planewaves, two characteristics came to the fore. Both were based in the spatial frequencies embedded onto the planewave by the scintillation effects of the plasma, and both produced reinforcing results that are in-line with previous research. Simply increasing scintillation expanded the high frequency content of the intensity variations' Fourier transform, producing a growing plateau within the Fourier plot. The two metrics for Sporadic-E analysis are two major features of this plateau: the final plateau frequency before it falls into the noise floor, and the slope at which that fall-off occurs, known as the spectral slope.

Both the slope and final frequency displayed the same tendencies: increasing blanking frequency produced lineally increasing metric values. Increasing plasma width produced quadraticly *decreasing* values. This latter relationship highlighted a key behavior that emerged continuously in the simulations (and is one noted in previous research): the rate of change of index of refraction (a result of altering it's geometric profile) produces dramatic changes in scintillation strength. Given the chaotic shape of real-world Sporadic-E clouds, understanding how this rate variance

affects radio occultation will be key in using this technique to characterize the ionospheric conditions.

The next stage of this research is two-fold: first applying the metrics derived from the Fourier transform to data collected from COSMIC and other RO sources. It is an open question of how well these metrics will fare in noisy environments. While the final plateau frequency metric seems to be fairly noise resistant, the spectral slope is far more vulnerable and it is far from certain that it will be useful under real-world conditions.

There is more work on the simulation side as well: the simulations here are somewhat crude, they do not take into account the true variation in Sporadic-E shape or orientation. Nor do they correct for planetary curvature, or other atmospheric effects. Additionally the precise limitations of the phase screen technique and its paraxial approximations are not explored here, and a full wave technique may need to be integrated to deal with reflections and small-scale fluctuations (finding that exact tipping point of where these fluctuations are important would be essential to determining when such a computationally expensive technique must be used).

There is clearly much more to be done in the field, but the metrics uncovered here will hopefully provide a useful tool to further exploration.

Bibliography

Arras, C. and Wickert, J. (2018). Estimation of ionospheric sporadic e intensities from GPS radio occultation measurements. *Journal of Atmospheric and Solar-Terrestrial Physics*, 171:60–63.

Beach, T. L., Pedersen, T. R., Starks, M. J., and Su, S.-Y. (2004). Estimating the amplitude scintillation index from sparsely sampled phase screen data. *Radio Science*, 39(5).

Carrano, C. S., Groves, K. M., Caton, R. G., Rino, C. L., and Straus, P. R. (2011). Multiple phase screen modeling of ionospheric scintillation along radio occultation raypaths. *Radio Science*, 46(6).

Davies, K. (1990). *Ionospheric Radio*. Peregrinus.

Denardini, C.M., Resende, L.C.A., and Moro, J. (2016). Occurrence of the blanketing sporadic-E layer during the recovery phase of the october 2003 superstorm. *Earth Planet*, 68(80).

Gooch, J. Y., Colman, J. J., Nava, O. A., and Emmons, D. J. (2020). Global ionosonde and gps radio occultation sporadic-e intensity and height comparison. *Journal of Atmospheric and Solar-Terrestrial Physics*, page 105200.

Group, S. I. W. (2010). White paper: Effect of ionospheric scintillations on gnss – a white paper. Technical report, Stanford Engineering GPS Lab, Stanford University, Stanford, California.

Hlubek, Nikolai, Berdermann, Jens, Wilken, Volker, Gewies, Stefan, Jakowski, Norbert, Wassaie, Mogese, and Damtie, Baylie (2014). Scintillations of the GPS,

glonass, and galileo signals at equatorial latitude. *J. Space Weather Space Clim.*, 4:A22.

Hocke, K., Igarashi, K., Nakamura, M., Wilkinson, P., Wu, J., Pavelyev, A., and Wickert, J. (2001). Global sounding of sporadic e layers by the GPS/met radio occultation experiment. *Journal of Atmospheric and Solar-Terrestrial Physics*, 63(18):1973–1980.

https://www.nesdis.noaa.gov/COSMIC-2 (2020). The NOAA national environmental satellite, data, and information service (NESDIS), COSMIC-2. `https://www.nesdis.noaa.gov/COSMIC-2`.

Hysell, D.L., Nossa, D.L., Aveiro, H.C., Larsen, M.F., Munro, J., Sulzer, M.P., and González, S.A. (2013). Fine structure in midlatitude sporadic e layers. *Journal of atmospheric and solar-terrestrial physics*, 103:16–23.

Joly, J. (1902). Mr. marconi's results in day and night wireless telegraphy. *Nature*, 66(199).

Kamp, M. v. d., Cannon, P. S., and Terkildsen, M. (2009). Effect of the ionosphere on defocusing of space-based radars. *Radio Science*, 44(1).

Knepp, D. (1982). Propagation of wide bandwidth signals through strongly turblulent ionized media. Technical Report DNA-TR-78, Defense Nuclear Agency Rep.

Knepp, D. (1983). Multiple phase-screen calculation of the temporal behavior of stochastic waves. *Proceedings of the IEEE*, 76(6):722–737.

Knepp, D. (2016). Multiple phase screen calculation of two-way spherical wave propagation in the ionosphere. *Radio Science*, 51:259–270.

Leontovich, M. and Fock, V. (1946). Solution of the problem of propagation of electromagnetic waves along the earth's surface by method of parabolic equations. *Journal of Physics-USSR*, 10:13–23.

Levy, M. (2000). *Parabolic equation methods for electromagnetic analysis wave propagation*. Institution of Electrical Engineers.

Maeda, J. and Heki, K. (2014). Two-dimensional observations of midlatitude sporadic e irregularities with a dense GPS array in japan. *Radio Science*, 49(1):28–35.

Maeda, J. and Heki, K. (2015). Morphology and dynamics of daytime mid-latitude sporadic-E patches revealed by GPS total electron content observations in japan. *Earth, Planets, and Space*, 67(89).

Maeda, J., Suzuki, T., Furuya, M., and Heki, K. (2016). Imaging the midlatitude sporadic e plasma patches with a coordinated observation of spaceborne insar and GPS total electron content. *Geophysical Research Letters*, 43(4):1419–1425.

Mathews, J. (1998). Sporadic-E: current views and recent progress. *Journal of atmospheric and solar-terrestrial physics*, 60(4):413–435.

McNeil, W. J., Dressler, R. A., and Murad, E. (2001). Impact of a major meteor storm on earth's ionosphere: A modeling study. *Journal of Geophysical Research: Space Physics*, 106(A6):10447–10465.

Rino, C. (2011). *The theory of scintillation with applications in remote sensing*. Wiley-IEEE Press.

Schafer, R. W. (2011). What is a Savitzky-Golay Filter? [lecture notes]. *IEEE Signal Processing Magazine*, 28(4):111–117.

Schunk, R. and Nagy, A. (2009). *Ionospheres: physics, plasma physics, and chemistry*. Cambridge University Press.

Singleton, D. G. (1970). Saturation and focusing effects in radio-star and satellite scintillations. *Journal of Atmospheric and Terrestrial Physics*, 32:187–208.

Thayaparan, T., Dupont, D., Ibrahim, Y., and Riddolls, R. (2019). High-frequency ionospheric monitoring system for over-the-horizon radar in Canada. *IEEE Transactions on Geoscience and Remote Sensing*, 57(9):6372–6384.

Whitehead, J. (1989). Recent work on mid-latitude and equatorial sporadic-E. *Journal of Atmospheric and Terrestrial Physics*, 51(5):401–424.

Wu, D. L., Ao, C. O., Hajj, G. A., de La Torre Juarez, M., and Mannucci, A. J. (2005). Sporadic-E morphology from GPS-CHAMP radio occultation. *Journal of Geophysical Research: Space Physics*, 110(A1).

Zeng, Z. and Sokolovskiy, S. (2010). Effect of sporadic E clouds on GPS radio occultation signals. *Geophysical Research Letters*, 37(18).

REPORT DOCUMENTATION PAGE

Form Approved
OMB No. 0704–0188

1. REPORT DATE *(DD–MM–YYYY)*	2. REPORT TYPE	3. DATES COVERED *(From — To)*
26–03–2020	Master's Thesis	May 2018 — Mar 2020

4. TITLE AND SUBTITLE

SIMULATION OF GPS RADIO OCCULTATIONS THROUGH SPORADIC-E USING THE MULTIPLE PHASE SCREEN METHOD

5a. CONTRACT NUMBER

5b. GRANT NUMBER

5c. PROGRAM ELEMENT NUMBER

6. AUTHOR(S)

Stambovsky, Daniel William, Capt, USAF

5d. PROJECT NUMBER

5e. TASK NUMBER

5f. WORK UNIT NUMBER

7. PERFORMING ORGANIZATION NAME(S) AND ADDRESS(ES)

Air Force Institute of Technology
Graduate School of Engineering and Management (AFIT/EN)
2950 Hobson Way
WPAFB OH 45433-7765

8. PERFORMING ORGANIZATION REPORT NUMBER

AFIT-ENP-MS-20-M-117

9. SPONSORING / MONITORING AGENCY NAME(S) AND ADDRESS(ES)

Air Force Research Laboratory/Space Vehicles
3550 Aberdeen Avenue SE
Kirtland AFB, NM 87117
DSN 246-3172, COMM 505-846-3172
Email: jonah.colman.1@us.af.mil

10. SPONSOR/MONITOR'S ACRONYM(S)

AFRL/RV

11. SPONSOR/MONITOR'S REPORT NUMBER(S)

12. DISTRIBUTION / AVAILABILITY STATEMENT

DISTRIBUTION STATEMENT A:
APPROVED FOR PUBLIC RELEASE; DISTRIBUTION UNLIMITED.

13. SUPPLEMENTARY NOTES

14. ABSTRACT

A phase screen simulation experiment is designed and implemented to model radio occultation through sporadic-E ionospheric disturbances between a GPS transmitter operating at the L1 frequency and a second receiving satellite in low earth orbit (LEO). Simulations were made to test the linear relationship between plasma intensity and scintillation S_4 index both posited (Arras and Wickert, 2018) and contended (Gooch et al., 2020) in previous literature. Results brought into question both the linear relationship and the use of S_4 as a whole and an alternate metric was sought. The current work points to two attributes of the low frequency plateau of the spatial Fourier transform of the $|\vec{E}|^2$ intensity as replacements for the the S_4 index. These metrics are shown to have direct relationships to key parameters of the Sporadic-E being simulated, reinforce each other, and have expected behavior under varying plasma conditions. Finally one of the proposed metrics (final peak frequency of the low-frequency plateau) is shown to be highly resistant to noise in the applied signal, and uncovers a promising as a path towards quickly analyzing radio occultation data.

15. SUBJECT TERMS

GPS Radio Occultation, Sporadic-E, Ionosphere

16. SECURITY CLASSIFICATION OF:			17. LIMITATION OF ABSTRACT	18. NUMBER OF PAGES	19a. NAME OF RESPONSIBLE PERSON
a. REPORT	b. ABSTRACT	c. THIS PAGE			Maj Daniel J. Emmons, AFIT/ENP
U	U	U	U	72	19b. TELEPHONE NUMBER *(include area code)* (937) 255-3636, x4571; Daniel.Emmons@afit.edu